



HAL
open science

Decompression-induced crystallization in hydrated silica-rich melts: Empirical models of experimental plagioclase nucleation and growth kinetics

Edith Mollard, Caroline Martel, Jean-Louis Bourdier

► **To cite this version:**

Edith Mollard, Caroline Martel, Jean-Louis Bourdier. Decompression-induced crystallization in hydrated silica-rich melts: Empirical models of experimental plagioclase nucleation and growth kinetics. *Journal of Petrology*, 2012, 53 (8), pp.1743-1766. 10.1093/petrology/egs031 . insu-00688849

HAL Id: insu-00688849

<https://insu.hal.science/insu-00688849>

Submitted on 13 Dec 2016

HAL is a multi-disciplinary open access archive for the deposit and dissemination of scientific research documents, whether they are published or not. The documents may come from teaching and research institutions in France or abroad, or from public or private research centers.

L'archive ouverte pluridisciplinaire **HAL**, est destinée au dépôt et à la diffusion de documents scientifiques de niveau recherche, publiés ou non, émanant des établissements d'enseignement et de recherche français ou étrangers, des laboratoires publics ou privés.



Distributed under a Creative Commons Attribution - NonCommercial - NoDerivatives 4.0 International License

Decompression-induced Crystallization in Hydrated Silica-rich Melts: Empirical Models of Experimental Plagioclase Nucleation and Growth Kinetics

EDITH MOLLARD^{1,2}, CAROLINE MARTEL^{1,2*} AND JEAN-LOUIS BOURDIER^{1,2}

¹UNIVERSITÉ ORLÉANS, ISTO, UMR 7327, 45071, ORLÉANS, FRANCE

²CNRS/INSU, ISTO, UMR 7327, 45071 ORLÉANS, FRANCE

**RECEIVED APRIL 6, 2011; ACCEPTED APRIL 18, 2012
ADVANCE ACCESS PUBLICATION JUNE 21, 2012**

Isothermal and isobaric crystallization of plagioclase in a water-saturated synthetic rhyolitic melt is investigated through a time-series of decompression experiments. The experimental variables are the rate at which samples are initially decompressed (30, 150, and 1200 MPa h⁻¹) from 200 MPa and 875°C, final pressure (25–160 MPa), and holding time at final pressure (up to 17 days). Through textural measurements of the crystals, plagioclase crystallization kinetics is characterized in terms of nucleation lag and rates of nucleation and growth. Plagioclase crystallization is markedly dependent on effective undercooling, ΔT_{eff} and holding time at crystallization pressure. With ΔT_{eff} increasing from 55 to 110°C, (1) nucleation lag decreases from 1–2 days to ~15 min, (2) maximum nucleation rates increase from $\sim 10^{-3}$ to 10^{-2} mm⁻² s⁻¹, and (3) maximum growth rates decrease from $\sim 10^{-6}$ to 5×10^{-7} mm s⁻¹. The initial decompression rate (30, 150, and 1200 MPa h⁻¹) has no systematic control on crystallization at final pressure, except for the 1200 MPa h⁻¹ series in which samples show nucleation difficulties. From the experimental data for ΔT_{eff} -constrained plagioclase number density, proportion, and morphology, we provide means to assess the conditions of nucleation and growth of natural plagioclase microlites from rapidly ascended rhyolitic melts, through the determination of the plagioclase liquidus curve and ΔT_{eff} prevailing during crystallization.

KEY WORDS: crystallization; plagioclase; nucleation delay; growth rate; effective undercooling

INTRODUCTION

Most andesitic to rhyolitic island-arc volcanoes are characterized by repeated episodes of effusive dome growth and explosive eruptions, such as dome destabilization into more or less violent pyroclastic flows or Plinian events (Roobol & Smith, 1976; Mullineaux & Crandell, 1981; Newhall *et al.*, 1996; Wolf & Eichelberger, 1997; Young *et al.*, 1998; Rutherford & Gardner, 2000). The occurrence of either type of eruptive behavior mainly reflects differences in magma degassing in response to variable ascent rates of the magma in the volcanic conduit (Jaupart & Allègre, 1991; Woods & Koyaguchi, 1994; Rutherford, 2008), which has prompted many studies on the degassing conditions and kinetics in silicic magmas (e.g. Sparks, 1978; Eichelberger *et al.*, 1986; Toramaru, 1989; Navon *et al.*, 1998; Gardner *et al.*, 1999; Melnik & Sparks, 1999; Martel & Bureau, 2001; Mourtada-Bonnefoi & Laporte, 2002, 2004; Gondé *et al.*, 2011). However, gas exsolution from a melt induces crystallization through an increase of the liquidus temperature (Tuttle & Bowen, 1958), provided enough time is available for crystallization. A number of studies have demonstrated that microlite crystallization occurs on eruptive timescales (Geschwind & Rutherford, 1995; Hammer & Rutherford, 2002; Martel & Schmidt, 2003; Brugger & Hammer, 2010). Nevertheless, the role of syn-eruptive crystallization in magma ascent conditions

and the explosive potential of the magma still remains unclear.

Most crystal nucleation and growth studies have been conducted in compositionally simple systems (Davis *et al.*, 1997; James *et al.*, 1997) and induced by cooling (Fenn, 1977; Donaldson, 1979; Tsuchiyama, 1983; Muncill & Lasaga, 1987, 1988; Roskosz *et al.*, 2005; Pupier *et al.*, 2008). In cooling conditions, the supersaturation required for crystallization is obtained by lowering the melt temperature with respect to the saturation (liquidus) temperature; that is, by increasing undercooling ($\Delta T = \text{crystal liquidus temperature} - \text{magma temperature}$). However, the driving force for crystallization in ascending silicic liquids may not be cooling, but melt dehydration as pressure decreases. The liquidus temperature of anhydrous crystals increases with decreasing melt water content. Therefore, isothermal depressurization of water-saturated liquids (decrease of melt water content) leads to an increasing difference between the crystal liquidus temperature and the magma temperature, referred as to the effective undercooling, ΔT_{eff} (Hammer & Rutherford, 2002). ΔT_{eff} directly controls the rates of crystal nucleation and growth, variations in which are reflected in specific crystal textures and morphologies (Lofgren, 1974, 1980; Brandeis & Jaupart, 1987; Roselle *et al.*, 1997; Hort, 1998; Toramaru, 2001; Hammer & Rutherford, 2002; Couch *et al.*, 2003; Hammer, 2004; Brugger & Hammer, 2010; Martel, 2012).

To provide reliable correlations between crystal characteristics (texture, morphology, and composition) and syn-eruptive crystallization conditions, we performed decompression-induced time-series experiments starting with a water-saturated silicic melt. We chose a simplified melt composition (four components) to (1) focus on plagioclase crystallization only, (2) reduce the number and complexity of the parameters controlling crystallization, and (3) facilitate crystallization thermodynamic modeling (to be reported elsewhere). In comparison with previous experimental studies (Hammer & Rutherford, 2002; Couch *et al.*, 2003; Brugger *et al.*, 2010), our starting samples were crystal-free; they were specifically designed to investigate homogeneous crystal nucleation and to discriminate the contribution of crystal nucleation from growth. These experiments are meant to qualitatively and quantitatively characterize the processes and rates of nucleation and growth as a function of ΔT_{eff} and pre-crystallization decompression rate.

EXPERIMENTAL AND ANALYTICAL METHODS

Starting material

The starting glass is a haplotonalite synthesized by Schott-AG (Germany) by mixing appropriate amounts of SiO_2 , $\text{Al}(\text{OH})_3$, CaCO_3 , NaNO_3 , and Na_2CO_3 , fusing at

1750°C for ~ 24 h while stirring, and cooling to 600°C at a rate of 20°C h^{-1} before air quenching. This crystal-free and bubble-free glass, hereafter referred to as HTND, has the following composition in wt %: 78.7 SiO_2 , 14.1 Al_2O_3 , 5.4 Na_2O , and 1.8 CaO (CIPW norm in wt %: 44 Quartz, 45 Albite, 9 Anorthite, 2 Corundum). The SiO_2 content of HTND is about 2 wt % higher than that of most of the rhyolitic interstitial glasses of common andesites to dacites (e.g. the microlite-free rhyolitic interstitial glass from the andesite of Mt Pelée, Martinique, contains 76–77 wt % SiO_2 ; Martel *et al.*, 1998). Therefore, HTND may be considered as a silicic end-member proxy for natural rhyolitic melts. Such a simplified composition is an acceptable compromise between natural and experimental requirements, in the sense that it (1) crystallizes nearly exclusively plagioclase, the major microlite phase of most of the natural rhyolites and (2) facilitates further thermodynamic modeling from experimental data.

Experimental device and method

To simulate decompression-driven isobaric crystallization in silicic melts under relevant volcanic conditions, we defined our experimental parameters in agreement with the pre-eruptive conditions proposed for the Mt Pelée plumbing system; that is, 200 MPa, 875°C, and melt water-saturation (Martel *et al.*, 1998).

Melt hydration

Hydrated glasses were prepared by mixing ~ 300 mg of finely ground HTND and enough distilled and deionized water to ensure saturation at 875°C and 200 MPa (i.e. 5.8 wt % calculated after Newman & Lowenstern, 2002). The water–glass mixtures were loaded in gold capsules (40 mm in length, 4.0 mm ID, 4.4 mm OD) and arc-welded shut. The capsules were held for at least 1 h in a drying oven at 120°C to homogenize water distribution and loaded in an internally heated pressure vessel (IHPV; ISTO, Orléans, France) for hydration at 875°C and 200 MPa over 1 week. The vertically working IHPV was pressurized with pure argon. Pressure (± 2 MPa) was monitored by a high-pressure transducer calibrated against a 700 MPa Heise gauge and temperature ($\pm 4^\circ\text{C}$) was monitored by K-type thermocouples. The samples were quenched isobarically to avoid water exsolution from the melt. Melt water saturation was confirmed by the presence of a droplet of excess water when opening the capsules.

Decompression experiments

Around 20–30 mg of hydrated HTND chips were loaded in gold capsules (~ 25 mm in length, 2.5 mm ID, 2.9 mm OD) and welded shut for dynamic decompression experiments in horizontally working cold-seal pressure vessels (CSPV; ISTO, Orléans, France) made of Inconel 100 (Ni-steel alloy) and pressurized with pure argon. Before each run, the furnaces of the CSPVs were calibrated at

the pressure of interest by internal (two reading points) and external (one reading point) K-type thermocouples (both types with precision of $\pm 4^\circ\text{C}$), to determine a hot-spot zone, ~ 3 cm long, without a significant temperature gradient. During an experiment, the sample temperature was read by only the external thermocouple (cumulative uncertainty of $\pm 8^\circ\text{C}$). Pressure (± 2 MPa) was monitored by a high-pressure transducer (Asco Instrument PR 851) calibrated against a 700 MPa Heise gauge. The capsule containing the hydrated glass chips was introduced into the vessel with a Ni-steel alloy filler rod 80 mm long to reduce gas convection at high temperature, pressurized to target pressure and heated to 875°C (requiring continuous depressurization to maintain pressure constant while heating).

All samples were held for 6 h at 200 MPa and 875°C (liquidus condition), to ensure a relevant and comparable chemical and structural state of the melt before decompression. Following this equilibration stage, the samples were depressurized by manually bleeding a pressure valve from 200 MPa (initial pressure, P_i) to various final pressures (P_f) between 25 and 160 MPa. The decompression ($\Delta P = P_i - P_f$) path followed multiple instantaneous decompression steps of 5 MPa. The total durations (Δt) of decompression were 7.5 min, 1 h, and 5 h, corresponding to decompression rates ($\Delta P/\Delta t$) of 1200, 150, and 30 MPa h^{-1} , respectively. At P_f , holding times were from 0 to 17 days. At the end of each anneal step, the sample was quenched by removing the vessel from the furnace and shaking it vertically to let the capsule and the filler rod drop into the water-cooled part of the vessel ($< 50^\circ\text{C}$), inducing quench rates of the order of $25\text{--}50^\circ\text{C s}^{-1}$. Only samples with similar capsule weights before and after the run were considered for further analysis.

Liquidus experiments

Several runs were performed to locate the plagioclase liquidus, which is a prerequisite for the determination of ΔT_{eff} . For this purpose, hydrated HTND chips were sealed in Au capsules that were run either at 200 MPa in CSPV or at 50 MPa in IHPV. In both cases, pressure and temperature were kept constant for 6 days, which has been demonstrated to ensure chemical equilibrium in haplogranitic melts at 200 MPa, $700\text{--}900^\circ\text{C}$, and ~ 6 wt % H_2O (Holtz *et al.*, 1992).

Analytical techniques

Crystal detection

Pieces of slightly crushed run products were placed on a glass plate and covered with a drop of density liquid (1.47) to check for the presence of crystals using an optical microscope equipped with a quarter-wave ($\frac{1}{4} \lambda$) plate. Although having a resolution of only $\sim 2 \mu\text{m}$, this technique permits good crystal detection for very low crystallinity ($< 1\%$).

Other grains from the same runs were embedded in epoxy resin, polished and carbon-coated for crystal analysis using a JEOL JSM-6400 scanning electron microscope (SEM) operating at 20 keV accelerating voltage and 6 nA beam current. SEM has the advantage of allowing better spatial resolution ($\sim 0.5 \mu\text{m}$) than optical microscopy, but crystal detection in a poorly crystallized sample frequently failed for statistical reasons (only a small fraction of the whole sample is observed).

To check for the presence of crystals at the nanoscale, we observed the samples using a Philips CM20 transmission electron microscope (TEM; CEMHTI, Orléans, France), operating at 200 kV and equipped with an Oxford energy-dispersive spectroscopy (EDS) analyzer [following the method described by Martel *et al.* (2011)]. The starting HTND glass and the samples quenched just after decompression were first crushed in ethanol to obtain a suspension of small glass particles that were deposited onto a holey carbon film supported by a copper grid.

Phase composition

Chemical analyses of the crystals and residual glasses were obtained using a Cameca SX50 electron microprobe (EMP; BRGM-ISTO, Orléans, France). EMP analytical conditions were 15 keV accelerating voltage, 5 nA beam current, and 10 s counting time on the element peaks with a focused beam ($1\text{--}2 \mu\text{m}$ in diameter) for crystal analysis. The beam was defocused ($\sim 10 \mu\text{m}$ in diameter) and Na was analyzed first for glass analysis to minimize Na migration (Pichavant, 1987; Devine *et al.*, 1995). The analytical errors on the oxide analyses are 1% relative for SiO_2 and Al_2O_3 , 2% for CaO, and 5% for Na_2O .

Glass water content

Water contents of the experimental glasses were determined by the EMP ‘by-difference’ method using hydrated standard glasses, as described in Devine *et al.* (1995). To have standard glasses of the same composition as the run products (in particular in Na, the volatilization of which under the electron beam is proportional to glass water content), we prepared three hydrated glass standards by filling Pt capsules with 550 mg of the haplogranite glass powder + deionized water in nominal amounts of 1, 3, and 5 wt % (which covers our investigated range of water saturation pressures). Capsules were welded shut for hydration runs in the IHPV at 300 MPa and 1200°C for 7 days. After isobaric quenching, the crystal-free glasses were analysed for their water contents by Mettler Toledo DL37 Karl-Fischer Titration (ISTO, Orléans, France), following the procedure given by Behrens (1995). The glass standards have water contents of 1.2 ± 0.2 , 2.9 ± 0.2 , and 4.8 ± 0.2 wt % (average values of 3–5 analyses on each sample). These glass standards were analysed by EMP together with the samples (analytical conditions given above for glasses). The differences from 100 wt % of the

EMP analyses of the glass samples were calibrated against the glass standards to provide accurate water content estimations with overall uncertainties of ± 0.4 wt %.

Textural analysis

Principles

Textural analyses of the run products were performed on SEM images of the samples using ImageJ and SPO2003 open-source software (Launeau & Robin, 1996; Launeau & Cruden, 1998). Depending on sample crystallinity, variable numbers of SEM images were acquired, to include at least 50 crystals per sample (Hammer *et al.*, 2000; Couch *et al.*, 2003; Clarke *et al.*, 2007). Because of the high number of adjacent plagioclase grains, manual demarcation of the crystals was necessary before conversion into binary images.

Parameter definition

For each sample, textural analysis consisted of measuring the respective area of bubbles (B), crystals (C), and glass (G), as well as the number of crystals (N) and bubbles (N_b), to calculate:

$$\begin{aligned} \text{area crystallinity (\%): } \Phi &= [C/(G+C)] \times 100; \\ \text{area porosity (\%): } P &= [B/(B+G+C)] \times 100; \\ \text{crystal number density (mm}^{-2}\text{): } N_a &= N/(G+C); \\ \text{bubble number density (mm}^{-2}\text{): } N_{\text{bubble}} &= N_b/(G+C); \end{aligned}$$

crystal length (μm): $L/2$ = average of the 10 longest semi long-axes of the crystals viewed in planar sections (Hammer *et al.*, 1999).

Considering the longest crystals rather than the mean length of the bulk crystal population better approaches the true three-dimensional (3D) length of a homogeneous crystal-size population by minimizing cross-cutting effects (Higgins, 1994). Crystals that were cut by the image edges were included in the count of Φ and N_a , but not of $L/2$.

Uncertainties

For a given sample, the statistical uncertainty on N_a , Φ , and $L/2$ was defined by repeating analyses of different images. Additionally, the interlocked character and the tortuous morphologies of some plagioclase crystals made it difficult to distinguish single crystals, especially for runs at low crystallization pressure. Thus, to minimize subjectivity during N_a and $L/2$ analysis, a first counting (A) was carried out by considering adjacent aligned objects as a single crystal with tortuous (overgrowths) morphology (leading to a minimum value for N_a and a maximum value for $L/2$). A second counting (B) was performed by considering each staggered object as small single crystals (maximum N_a and minimum $L/2$). Because we do not have arguments in favour of one or the other counting method, we show the results given by both methods and define N_a and $L/2$ as the average values (Fig. 1).

3D conversion

We converted the planar major and minor axes of the crystals into 3D crystal habits using the spreadsheet program of Morgan & Jerram (2006). The program compares the 2D measurements of long and short axes for non-foliated objects with a database of 2D data obtained mathematically from random sections through 703 different habits (Short\Intermediate\Long axis ranging from 1\1\1 to 1\10\10). The output gives the five best-match curves and corresponding crystal habits based on a least-squares fit between sample and database. Morgan & Jerram suggested a minimum of ~ 200 crystal sections to robustly determine crystal habits if the crystals have acicular shapes, so that some of our textural analyses for which the crystal count is between 50 and 200 are subject to large errors, often resulting in poor square residuals ($R^2 < 0.65$).

RESULTS

Plagioclase liquidus location and effective undercooling (ΔT_{eff})

The samples from the phase equilibrium runs designed to locate the plagioclase liquidus were checked for the presence of crystals using optical microscopy, SEM and TEM. The results indicate that liquidus conditions are reached at 200 MPa between 850 and 875°C and at 50 MPa between 1000 and 1040°C (Table 1). Following similar crystal-hunting methods, we also constrained the liquidus at 875°C between 160 and 180 MPa from the decompression runs held for 7 days at P_f (Table 2). Assuming that the liquidus curves are approximately parallel for water-saturated rhyolitic melts with different normative An contents (Tuttle & Bowen, 1958; Hammer & Rutherford, 2002; Couch *et al.*, 2003; Martel, 2012), we located the HTND liquidus (normative An = 9 wt %) from our crystal-bearing and crystal-free experiments, by paralleling the plagioclase liquidus curve of a Mt Pelée rhyolitic melt (normative An = 12 wt %; Martel, 2012). The deduced ΔT_{eff} is $\sim 55^\circ\text{C}$ at 100 MPa, $\sim 110^\circ\text{C}$ at 50 MPa, and $\sim 175^\circ\text{C}$ at 25 MPa (Fig. 2).

Decompression-induced plagioclase crystallization

Crystal hunting using optical microscopy, SEM and TEM was performed on samples quenched just after decompression, to verify that plagioclase crystallization does not occur during decompression. All methods confirm crystal-free glasses when decompressed to $P_f = 50$ MPa ($t = 0$ at P_f), regardless of the decompression rate. This indicates that plagioclase nucleation actually proceeds isobarically during the anneal step at P_f , which provides a means to relate nucleation and growth kinetics to ΔT_{eff} for a given P_f , assuming equilibrium degassing (tested below).

CRYSTAL COUNTING METHOD

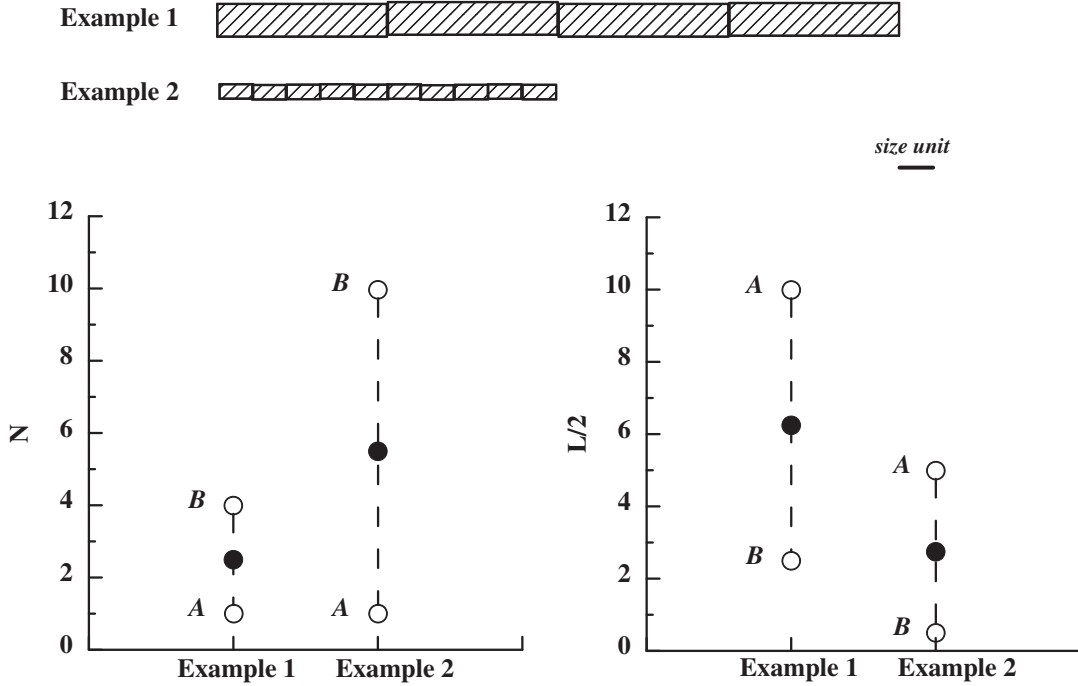


Fig. 1. Method of crystal demarcation and counting adopted for interlocked crystals. Count A considers the interlocked structures as a single crystal with overgrowths leading to a tortuous morphology, whereas count B considers aligned single crystals. Without arguments in favor of one or the other counting method, we defined the data point (filled symbols) as the mean between the values given by the two counting methods (open symbols).

Table 1: HTND liquidus experiments (water saturation)

Run no.	P (MPa)	T ($^{\circ}C$)	Time (day)	Plag	Method*
200A	200	850	6	Yes	OM, SEM
200B	200	875	6	No	OM, SEM, TEM
50A	50	1000	6	Yes	OM, SEM
50B	50	1040	6	No	OM, SEM

*Method used for crystal hunting: OM, optical microscopy; SEM, scanning electron microscopy; TEM, transmission electron microscopy.

The experimental conditions of the decompression experiments and the plagioclase textural analyses are reported in Table 2. Selected images of the decompression run products are shown in Fig. 3. The plagioclase and glass compositions are given in Table 3. The characteristics of plagioclase nucleation (delay, crystal number density), growth (crystal content and morphology), and composition are hereafter described as a function of P_f (or ΔT_{eff}),

pre-crystallization decompression rate, and annealing duration at P_f .

Crystallization at $P_f \geq 140$ MPa ($\Delta T_{eff} \leq 25^{\circ}C$)

The samples quenched at $P_f \geq 140$ MPa were decompressed at a rate of 1200 MPa h^{-1} . For a duration of 3 days at $P_f = 160$ MPa, N_a reaches 138 mm^{-2} , Φ is below 1%, and $L/2$ is $\sim 33 \mu\text{m}$. After 7 days at $P_f = 140$ MPa, N_a has a value of 22 mm^{-2} , Φ is below 1%, and $L/2$ is $\sim 67 \mu\text{m}$. At both P_f , plagioclase crystals are compact (fully crystallized) rectangular prisms (Fig. 3a and b) with axis dimensions of $1.5 \setminus 10$.

Plagioclase composition is $\text{An}_{43 \pm 1}$ and $\text{An}_{42 \pm 2}$ at 160 and 140 MPa, respectively, and the residual glasses have SiO_2 contents of 78–79 wt %, which are very close to the liquidus composition.

Crystallization at $P_f = 100$ MPa ($\Delta T_{eff} \sim 55^{\circ}C$)

Nucleation occurs between 1 and 2 days at 100 MPa (Table 2). Samples decompressed at a rate of 1200 MPa h^{-1} show N_a below 50 mm^{-2} , reaching 100 and

Table 2: Experimental conditions of the decompression runs and plagioclase textural analyses

Experimental conditions				Analytical results					
$(P_i = 200 \text{ MPa}, T = 875^\circ\text{C})^*$				Two dimensions [†]			Three dimensions [‡]		
Run no.	P_f (MPa)	$\Delta P/\Delta t$ (MPa h ⁻¹)	Time at P_f (day)	Φ (%)	N_a (mm ⁻²)	$L/2$ (μm)	S\ L axis	R^2	Shape
195/1200/1	195	1200	1	0	0	0			
190/1200/0.65	190	1200	0.65	0	0	0			
190/1200/2	190	1200	2	0	0	0			
180/1200/2	180	1200	2	0	0	0			
180/1200/7	180	1200	7	0	0	0			
160/1200/1	160	1200	1	0	0	0			
160/1200/2	160	1200	2	0	0	0			
160/1200/3	160	1200	3	0.7 (0.9)	138 (3)	33 (2)	1\5\10	0.57	rect prism
160/1200/7	160	1200	7	traces	traces	n.d.	n.d.	n.d.	n.d.
140/1200/2	140	1200	2	traces	traces	n.d.	n.d.	n.d.	n.d.
140/1200/7	140	1200	7	0.6 (0.9)	22 (3)	67 (2)	n.d.	n.d.	n.d.
100/1200/1	100	1200	1	0	0	0			
100/1200/2	100	1200	2	1.4 (1.1)	30 (3)	58 (2)	n.d.	n.d.	n.d.
100/1200/3	100	1200	3	0.4 (0.9)	14 (3)	50 (2)	n.d.	n.d.	n.d.
100/1200/4	100	1200	4	1.3 (1.0)	19 (3)	67 (2)	1\10\10	0.81	rect prism
100/1200/7	100	1200	7	0.8 (0.9)	16 (3)	66 (2)	n.d.	n.d.	n.d.
100/150/2	100	150	2	2.4 (1.3)	50 (7)	63 (5)	n.d.	n.d.	n.d.
100/150/4	100	150	4	9.4 (2.4)	174 (23)	78 (9)	1\5\10	0.72	rect prism
100/150/7	100	150	7	10.2 (2.5)	270 (51)	74 (4)	1\6\10	0.88	rect prism
100/30/4	100	30	4	6.9 (2.1)	116 (13)	91 (17)	1\5\10	0.78	rect prism
100/30/7	100	30	7	10.5 (2.6)	105 (18)	91 (10)	1\6\10	0.71	rect prism
75/1200/0.5	75	1200	0.5	0	0	0			
75/1200/1	75	1200	1	1.7 (0.9)	22 (3)	18 (3)	n.d.	n.d.	n.d.
75/1200/2	75	1200	2	2.4 (1.3)	74 (8)	40 (6)	n.d.	n.d.	n.d.
75/1200/7	75	1200	7	13.2 (2.8)	158 (21)	83 (13)	n.d.	n.d.	n.d.
75/1200/17	75	1200	17	16.4 (3.1)	185 (52)	101 (20)	1\3.2\10	0.57	acicular
75/150/2	75	150	2	4.5 (1.7)	106 (11)	37 (2)	1\2\10	0.62	acicular
75/150/4	75	150	4	13.0 (2.8)	361 (47)	50 (10)	n.d.	n.d.	n.d.
75/150/7	75	150	7	17.2 (3.2)	244 (33)	66 (12)	1\1.6\10	0.66	acicular
75/150/17	75	150	17	17.6 (3.2)	411 (60)	67 (9)	1\4\10	0.83	rect prism
75/30/2	75	30	2	9.5 (2.4)	249 (37)	59 (3)	1\2.2\8	0.63	acicular
75/30/4	75	30	4	12.7 (2.8)	326 (45)	65 (1)	1\3.4\9	0.65	acicular
75/30/7	75	30	7	19.1 (3.2)	500 (52)	75 (1)	1\3.4\10	0.66	acicular
75/30/17	75	30	17	18.4 (3.2)	169 (22)	80 (22)	n.d.	n.d.	n.d.
50/1200/0	50	1200	0	0	0	0			
50/1200/0.25	50	1200	0.25	0.1 (0.8)	84 (7)	12 (1)	1\4.5\10	0.81	rect prism
50/1200/0.65	50	1200	0.65	0.4 (0.9)	129 (38)	28 (9)	1\4\10	0.76	acicular
50/1200/1	50	1200	1	1.0 (1.0)	200 (70)	37 (22)	1\4.5\10	0.67	rect prism
50/1200/2	50	1200	2	4.2 (1.6)	205 (81)	81 (58)	1\2.5\10	0.74	acicular
50/1200/7	50	1200	7	20.3 (3.3)	1160 (312)	62 (15)	1\2.5\9	0.71	acicular
50/1200/17	50	1200	17	21.4 (3.3)	423 (118)	107 (47)	1\3\10	0.74	acicular

(continued)

Table 2: Continued

Experimental conditions				Analytical results					
$(P_f = 200 \text{ MPa}, T = 875^\circ \text{C})^*$				Two dimensions [†]			Three dimensions [‡]		
Run no.	P_f (MPa)	$\Delta P/\Delta t$ (MPa h ⁻¹)	Time at P_f (day)	Φ (%)	N_a (mm ⁻²)	$L/2$ (μm)	S\ L axis	R^2	Shape
50/150/0	50	150	0	0	0	0			
50/150/2	50	150	2	6.9 (2.1)	536 (152)	36 (5)	1\ 1.9\ 10	0.75	rect prism
50/150/4	50	150	4	20.5 (3.3)	956(245)	50(16)	1\ 2.5\ 9	0.73	acicular
50/150/17	50	150	17	24.2 (3.3)	996 (181)	44 (8)	1\ 3.4\ 9	0.65	acicular
50/30/0	50	30	0	0	0	0			
50/30/0.74	50	30	0.74	0.1 (0.4)	27 (6)	13.1 (2)	n.d.	n.d.	n.d.
50/30/2	50	30	2	7.1 (2.1)	664 (237)	44 (9)	1\ 2.7\ 8	0.69	acicular
50/30/4	50	30	4	15.9 (3.1)	1334 (481)	51 (13)	1\ 2.3\ 9	0.69	rect prism
50/30/7	50	30	7	19.9 (3.3)	1007 (232)	57 (1)	1\ 2.8\ 8	0.75	acicular
50/30/17	50	30	17	20.4 (3.3)	786 (304)	48 (2)	1\ 2.7\ 8	0.65	rect prism
25/1200/0.65	25	1200	0.65	< 1	n.d.	n.d.	n.d.	n.d.	dendrite
25/1200/1	25	1200	1		n.d.	n.d.	n.d.	n.d.	dendrite
25/1200/2	25	1200	2	~3 (2)	~1400 (500)	~40 (5)	n.d.	n.d.	dendrite
25/1200/7	25	1200	7		n.d.	n.d.	n.d.	n.d.	dendrite

* P_f is final pressure; $\Delta P/\Delta t$ is decompression rate; time gives anneal duration at P_f .

[†]Planar plagioclase analyses; Φ is area crystallinity; N_a is crystal number density; $L/2$ is average length of the 10 longest semi-axes of the crystals, as defined in the text. The 2σ uncertainty is given in parentheses.

[‡]SIL axis gives the short, intermediate, and long axis calculated after Morgan & Jerram (2006) from the 2D long and short axes. R^2 gives residual square; Shape gives the 3D habit (rectangular prism, acicular or dendrite).

n.d., not determined.

~300 mm⁻² for decompression rates of 30 and 150 MPa h⁻¹, respectively (Fig. 4a).

Samples decompressed at a rate of 1200 MPa h⁻¹ have Φ remaining below 2% (Fig. 4b). For slower decompression rates, Φ significantly increases for 2–3 days following nucleation and reaches a plateau at ~10%. Plagioclase $L/2$ increases for 2–3 days after nucleation and reaches a plateau value that increases from 65 to 95 μm as decompression rate decreases from 1200 to 30 MPa h⁻¹ (Fig. 4c). Plagioclases are rectangular prisms with hollow shapes (Fig. 3c, m–o), with crystal axis dimensions of about 1\|5–10\|10 (Table 2).

Plagioclase composition at $P_f = 100$ MPa is An_{37–39}, regardless of $\Delta P/\Delta t$ and duration at P_f (Fig. 5a). Residual glasses, however, show $\Delta P/\Delta t$ -dependent compositions. The samples decompressed at 1200 MPa h⁻¹ have glass SiO₂ contents comparable with the liquidus composition (i.e. 78–79 wt %) whereas those decompressed at rates of 30 and 150 MPa h⁻¹ contain SiO₂ up to ~81 wt % (Fig. 5b).

Crystallization at $P_f = 75$ MPa ($\Delta T_{\text{eff}} \sim 80^\circ \text{C}$)

At $P_f = 75$ MPa, the nucleation delay is between 0.5 and 1 day (Table 2). For the three decompression rates, N_a increases for about 6 days after nucleation. For

decompression rates of 1200 and 150 MPa, N_a reaches a plateau value of ~200 and 400 mm⁻², respectively. For the slower decompression rate of 30 MPa h⁻¹, however, N_a reaches a maximum value of ~500 mm⁻² and decreases to ~200 mm⁻² at 17 days (Fig. 4d).

Regardless of decompression rate, Φ increases for ~6 days following nucleation before reaching a plateau value between 15 and 20% (Fig. 4e). $L/2$ reaches plateau values between 65 and 100 μm for decompression rates between 30 and 1200 MPa h⁻¹ (Fig. 4f). Plagioclases have hollow acicular morphologies (Fig. 3d–f, p–r), with axis proportions around 1\|3–4\|9–10 (Table 2).

After decompression at rates of 1200 and 30 MPa h⁻¹, plagioclase composition is An_{32–35}, regardless of anneal duration, whereas the sample decompressed at 150 MPa h⁻¹ shows plagioclase An₃₀ after 17 days (Fig. 5c). The SiO₂ contents of the residual glasses reach a plateau value of ~82 wt % after 7 days (Fig. 5d).

Crystallization at $P_f = 50$ MPa ($\Delta T_{\text{eff}} \sim 110^\circ \text{C}$)

Runs carried out at $P_f = 50$ MPa with anneal durations < 1 day suggest nucleation onset within 6 h following decompression ($\Delta P/\Delta t$ of 1200 MPa h⁻¹; Table 2). N_a drastically increases for 4–5 days before reaching a maximum value

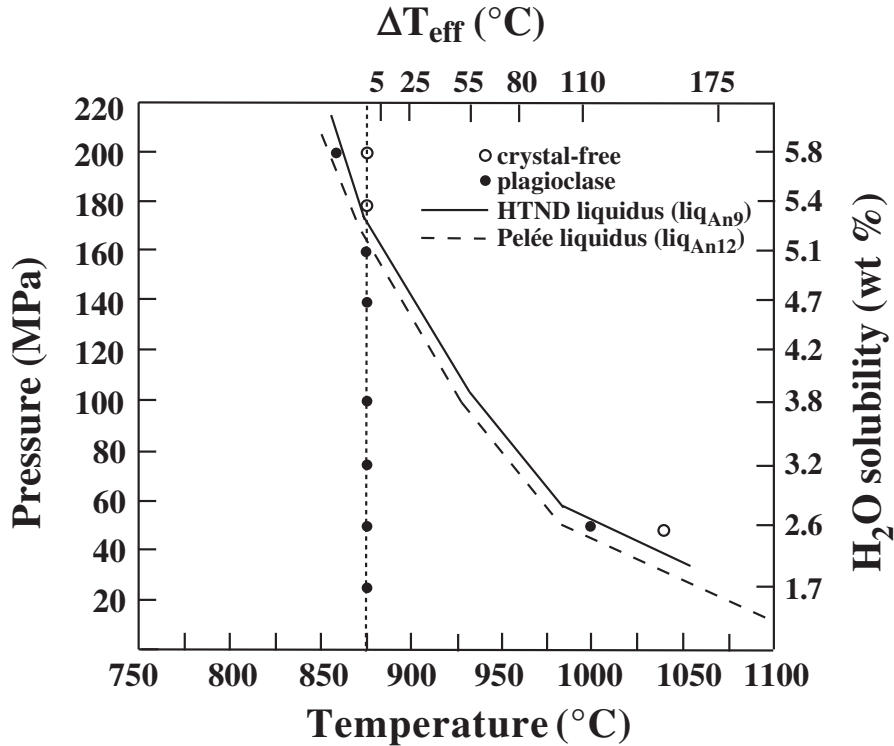


Fig. 2. Plagioclase liquidus for HTND, determined from crystal-free and plagioclase-bearing run products and drawn by paralleling the plagioclase liquidus of Mt Pelée rhyolitic melt (Martel, 2012). The upper x -axis gives the effective undercooling, ΔT_{eff} , as the temperature difference between the HTND liquidus and the run temperature (875°C). The right y -axis gives water solubility at pressure, calculated after Newman & Lowenstern (2002).

around 1000–1300 mm^{-2} . For decompression rates of 1200 and 30 MPa h^{-1} , N_a further decreases to ~ 400 and 700 mm^{-2} at 17 days, respectively, whereas N_a is maintained for the 150 MPa h^{-1} series (Fig. 4g). Counting crystals following method A (lowest values of N_a ; Fig. 1) does not change the fact that these curves pass through a maximum and further decrease, but the effect is reduced.

The time evolution of Φ does not vary within error as a function of $\Delta P/\Delta t$, increasing for ~ 7 days before reaching a plateau value between 18 and 22% (Fig. 4h). $L/2$ increases for ~ 4 days before reaching a plateau value of $\sim 55 \mu\text{m}$ for the samples decompressed at 30 and 150 MPa h^{-1} and $\sim 85 \mu\text{m}$ for the 1200 MPa h^{-1} series (Fig. 4i). Counting crystals following method B (lowest values of $L/2$; Fig. 1) would significantly reduce the size difference between the series (Fig. 4i), but the crystal size difference is still observable by comparing run 50/1200/17 (Fig. 3i) with run 50/30/17 (Fig. 3u). The crystals have hollow either rectangular prism or acicular morphologies (Fig. 3g–i, s–u), with axis proportions of 1\2.5–3.5\8–10 (Table 2).

Plagioclase compositions decrease from An_{30-32} at time < 2 days to $\sim \text{An}_{24-28}$ after 4 days (Fig. 5e). Glass compositions reach 81–82 wt % after 4–7 days and ~ 83 wt % after 17 days (Fig. 5f). A silica polymorph crystallizes at

between 2 and 4 days (Table 3), the texture of which, either botryoidal or pervasive, could be cristobalite (Hobblit & Harmon, 1993; Martel & Schmidt, 2003).

Crystallization at $P_f = 25 \text{ MPa}$ ($\Delta T_{\text{eff}} \sim 175^\circ \text{C}$)

Four samples were decompressed at $P_f = 25 \text{ MPa}$ ($\Delta P/\Delta t = 1200 \text{ MPa h}^{-1}$) with holding times of 16 h, 1, 2, and 4 days. They display highly heterogeneously distributed areas of dendritic plagioclase intermingled with the silica phase (Fig. 3j–l). Plagioclase textural analysis was particularly difficult owing to both the small size and the dendritic nature of the crystals. Our rough estimation for the sample held for 2 days at P_f gives $\Phi \sim 3 \pm 2\%$, $N_a \sim 1400 \text{ mm}^{-2}$, and $L/2 \sim 40 \mu\text{m}$ (Table 2). Plagioclases could not be analyzed by EMP, but the glass contains 78.5 wt % of SiO_2 (Table 3), which is close to the liquidus composition.

Empirical crystallization laws

Fit functions of the time evolution of N_a , Φ , and $L/2$

To provide nucleation and growth laws for plagioclase, the time evolutions of N_a , Φ , and $L/2$ were fitted using simple functions. Despite the fact that simple fit functions may not be constrained by the data as precisely as polynomial fits would be, they have the advantage of being

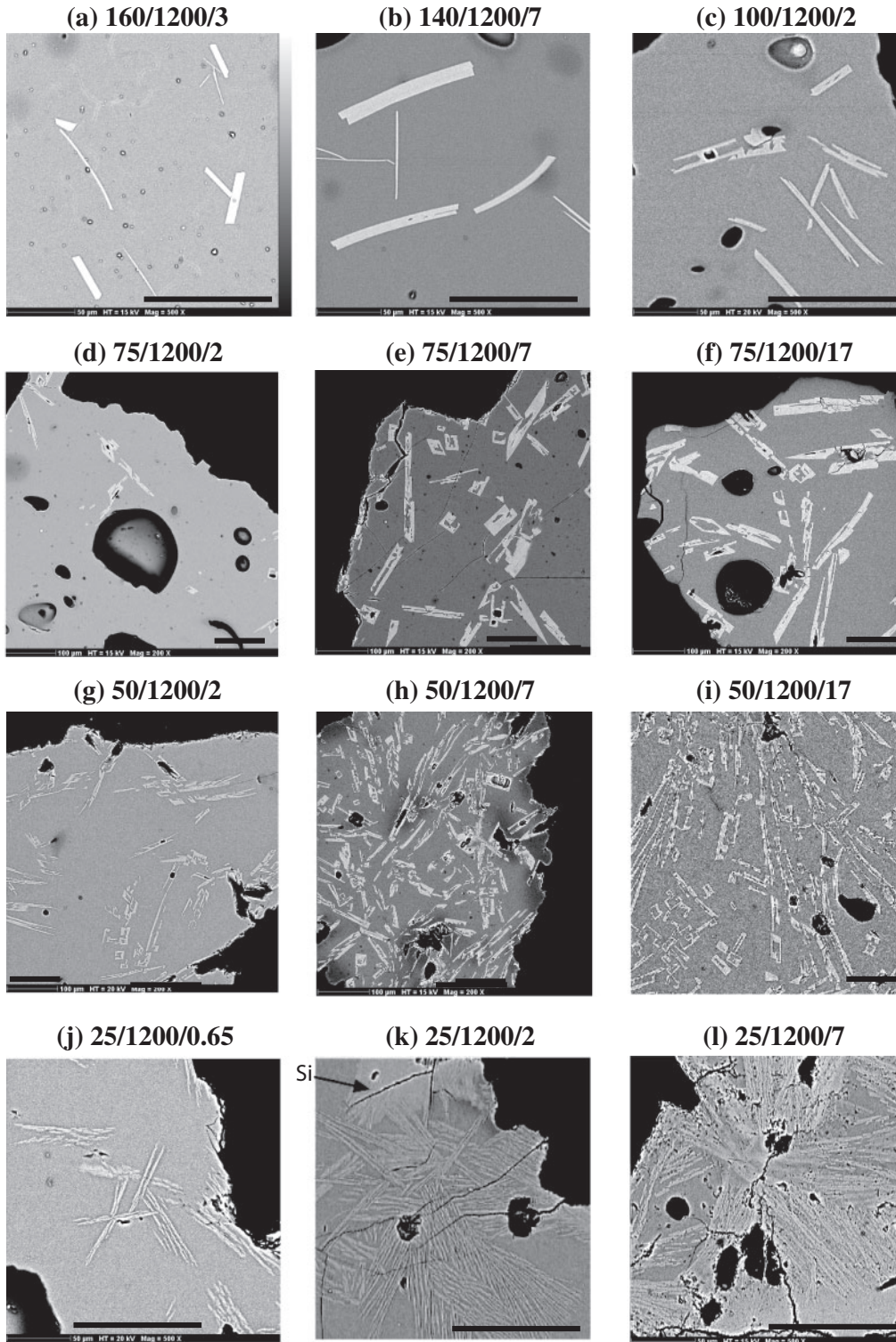


Fig. 3. Selected SEM images of the samples decompressed at 1200 MPa h^{-1} (a–l), at 150 MPa h^{-1} (m), and 30 MPa h^{-1} (n–u); run number as in Table 2. Light grey crystals are plagioclase, dark grey area is glass, and black is pore space. The scale bar represents $100 \mu\text{m}$ for all images. It should be noted that samples with $\Phi < 10\%$ (runs with durations < 4 days) mostly show heterogeneously distributed plagioclase, so that the selected images may not be representative of the texture of the whole sample.

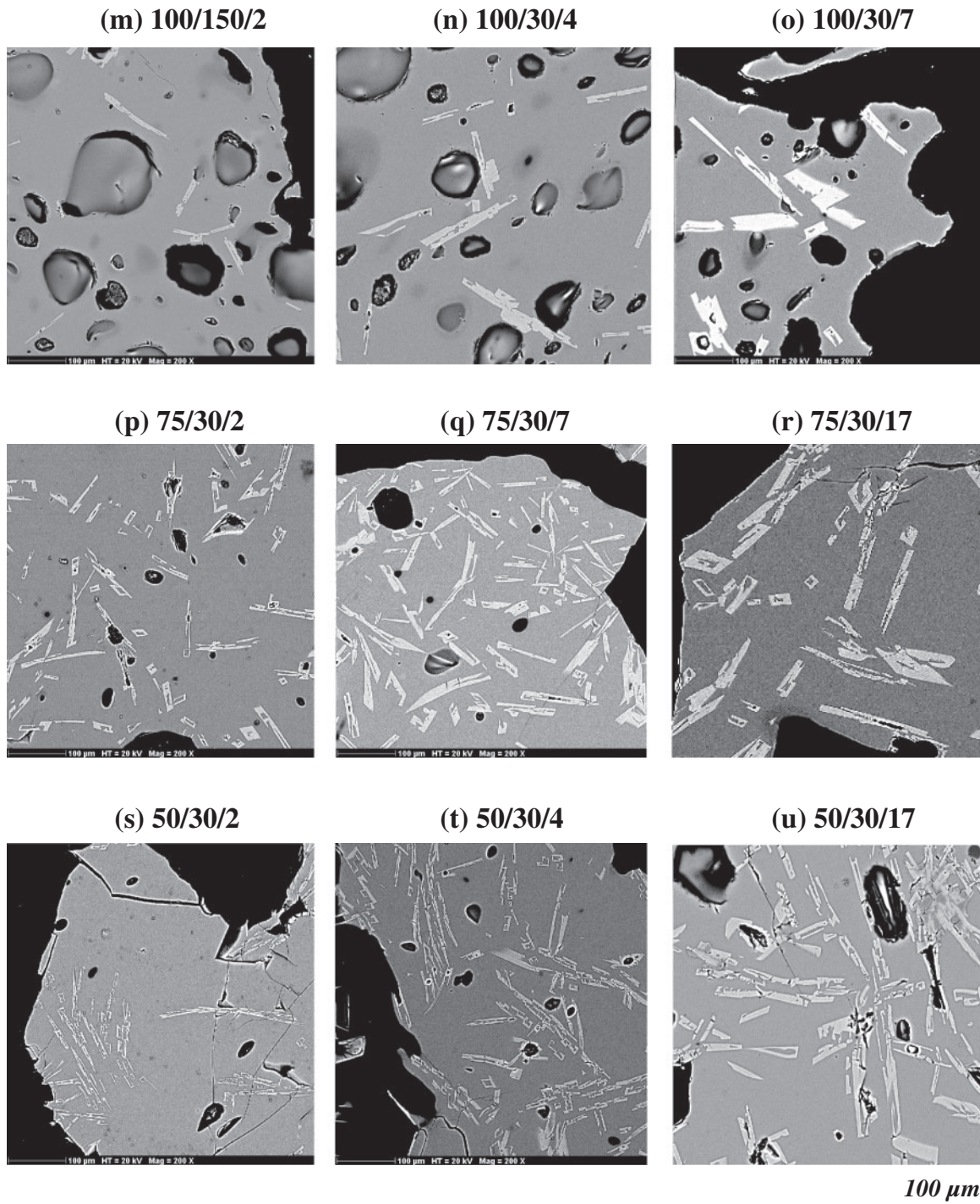


Fig. 3. Continued.

mathematically easily time-derived to obtain nucleation and growth rates. Essentially, this is an acceptable compromise between fitting accuracy and convenience for future modelling of the crystallization rates.

All time evolutions of N_a , Φ , and $L/2$ were fitted by square root of time functions relieved by a plateau value. At $P_f = 50$ MPa, the experiments performed at anneal durations < 2 days ($\Delta P/\Delta t = 1200$ MPa h $^{-1}$) suggest that the

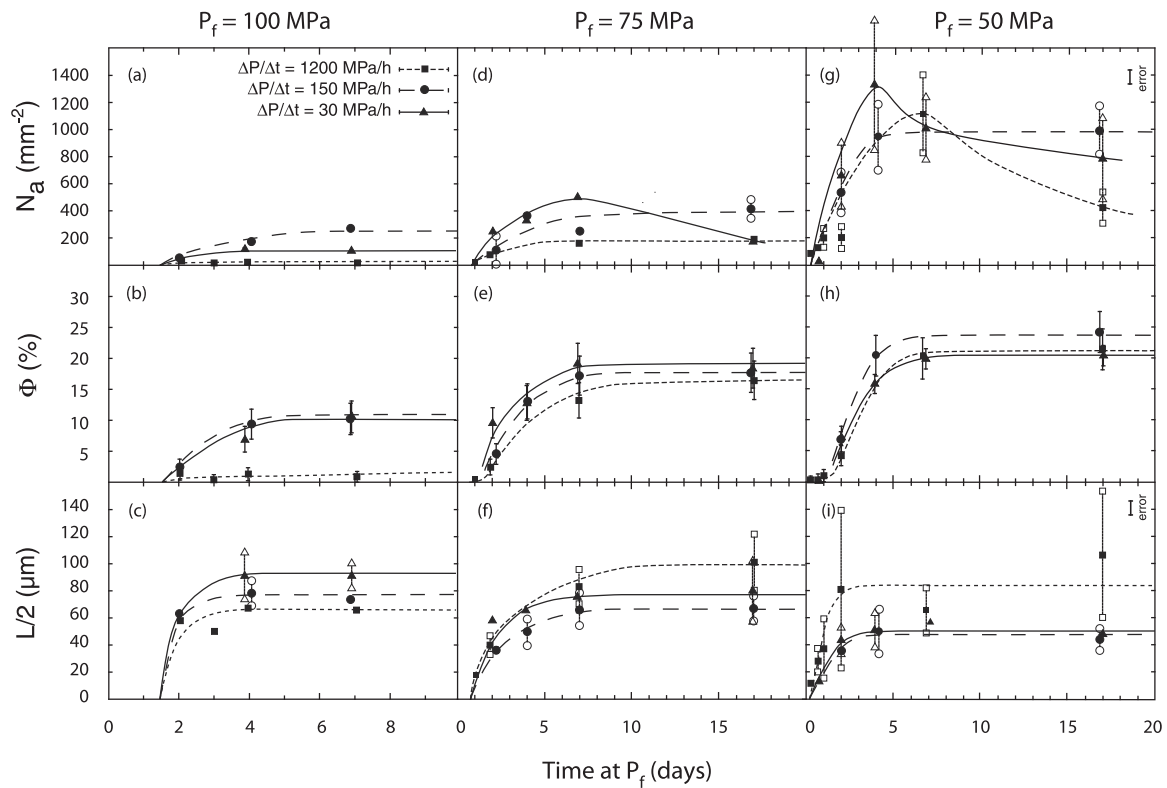


Fig. 4. Evolution of N_a , Φ , and $L/2$ as a function of $\Delta P/\Delta t$ and run duration at P_f for $P_f = 100$ MPa (a–c), 75 MPa (d–f), and 50 MPa (g–i). All data have been fitted using square roots of time functions followed by a plateau value; Φ data in (e) and (h) show starting exponential laws. Error bars give the statistical uncertainties and are included in the symbol size when not indicated, except for (g) and (i), in which the error bar is given in the upper right corner. In (g) and (i), open symbols show the results of the counting methods A and B, as described in Fig. 1.

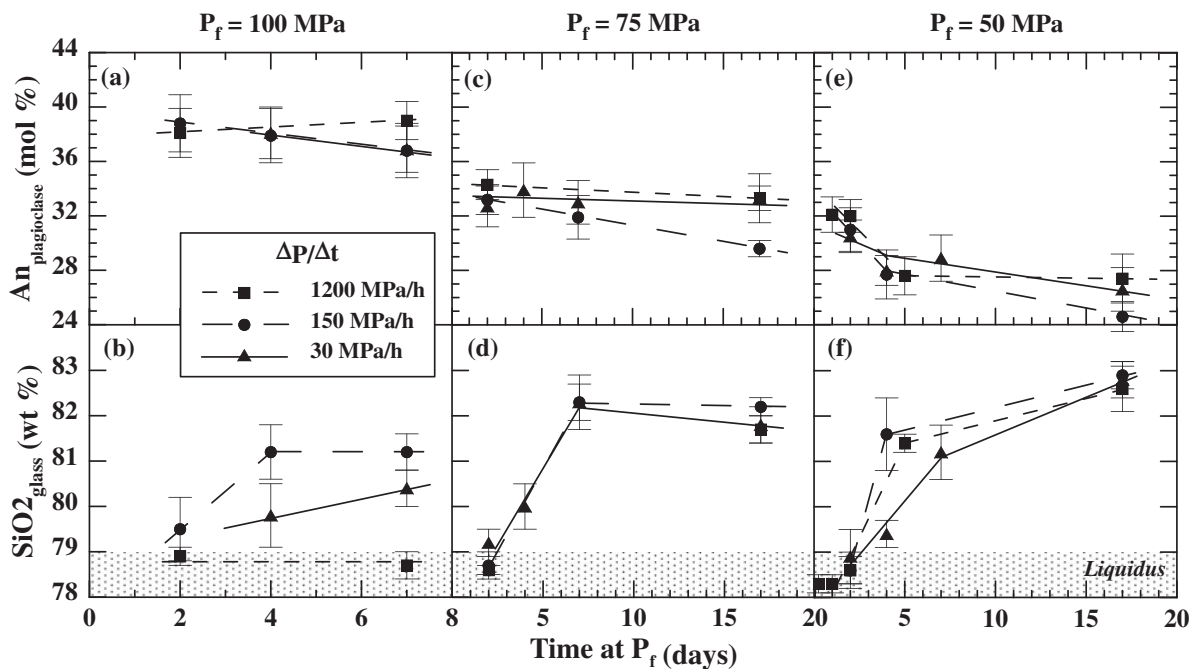


Fig. 5. Compositions of plagioclase (molar anorthite content) and residual glass (SiO_2 content) as a function of $\Delta P/\Delta t$ and run duration at P_f , for $P_f = 100$ MPa (a, b), 75 MPa (c, d), and 50 MPa (e, f).

Table 3: Chemical compositions of the phases

Run no. ¹	Phase ²	n^3	SiO ₂ ⁴	Al ₂ O ₃ ⁴	CaO ⁴	Na ₂ O ⁴	An (mol %) ⁵
200B	glass	7	78.7 (0.2)	14.1 (0.2)	1.8 (0.1)	5.4 (0.1)	
160/1200/3	plag	6	58.6 (0.6)	26.4 (0.3)	8.6 (0.3)	6.3 (0.1)	43.1 (1.1)
	glass	6	78.7 (0.1)	14.1 (0.1)	1.7 (0.1)	5.4 (0.2)	
140/1200/7	plag	6	58.5 (0.7)	26.3 (0.4)	8.7 (0.5)	6.5 (0.3)	42.3 (2.0)
	glass	6	78.8 (0.3)	14.0 (0.2)	1.7 (0.1)	5.5 (0.2)	
100/1200/2	plag	13	61.1 (1.3)	24.8 (0.9)	7.4 (0.5)	6.7 (0.2)	38.1 (1.8)
	glass	12	78.9 (0.2)	14.1 (0.1)	1.7 (0.1)	5.3 (0.2)	
100/1200/7	plag	7	59.6 (0.4)	25.6 (0.2)	7.9 (0.3)	6.8 (0.3)	39 (1.4)
	glass	6	78.7 (0.3)	14.2 (0.3)	1.7 (0.1)	5.5 (0.1)	
100/150/2	plag	8	60.0 (1.2)	25.3 (0.8)	7.8 (0.6)	6.8 (0.2)	38.8 (2.1)
	glass	9	79.5 (0.7)	13.7 (0.5)	1.6 (0.1)	5.2 (0.2)	
100/150/4	plag	6	59.6 (0.7)	25.6 (0.4)	7.8 (0.5)	7.0 (0.2)	37.9 (2.0)
	glass	6	81.2 (0.6)	12.7 (0.4)	1.2 (0.1)	4.9 (0.2)	
100/150/7	plag	10	60.5 (0.9)	25.1 (0.5)	7.4 (0.5)	7.0 (0.2)	36.8 (2.0)
	glass	9	81.2 (0.4)	12.6 (0.3)	1.1 (0.1)	5.1 (0.2)	
100/30/4	plag	8	60.0 (0.5)	25.4 (0.3)	7.7 (0.4)	6.9 (0.2)	38.1 (1.9)
	glass	8	79.8 (0.7)	13.8 (0.3)	1.4 (0.1)	5.0 (0.5)	
100/30/7	plag	5	60.6 (0.7)	24.9 (0.5)	7.4 (0.3)	7.0 (0.2)	36.9 (1.7)
	glass	6	80.4 (0.4)	12.9 (0.3)	1.2 (0.1)	5.4 (0.2)	
75/1200/2	plag	4	62.3 (0.6)	23.9 (0.4)	6.7 (0.1)	7.1 (0.3)	34.3 (1.1)
	glass	6	78.6 (0.1)	14.0 (0.1)	1.7 (0.1)	5.6 (0.2)	
75/1200/17	plag	5	61.1 (0.8)	24.7 (0.5)	6.7 (0.2)	7.5 (0.3)	33.3 (0.9)
	glass	7	81.7 (0.3)	12.1 (0.2)	0.8 (0.1)	5.3 (0.2)	
75/150/2	plag	9	61.2 (0.2)	24.6 (0.2)	6.8 (0.2)	7.5 (0.1)	33.2 (1.1)
	glass	8	78.7 (0.3)	14.2 (0.1)	1.7 (0.1)	5.5 (0.2)	
75/150/7	plag	7	61.3 (0.4)	24.5 (0.3)	6.5 (0.3)	7.7 (0.2)	31.9 (1.6)
	glass	7	82.3 (0.6)	12.1 (0.4)	0.8 (0.1)	4.8 (0.6)	
75/150/17	plag	7	61.6 (0.3)	24.3 (0.2)	6.1 (0.1)	8.0 (0.1)	29.6 (0.6)
	glass	8	82.2 (0.2)	11.9 (0.2)	0.7 (0.1)	5.2 (0.2)	
75/30/2	plag	4	62.7 (1.1)	23.6 (0.8)	6.4 (0.2)	7.3 (0.4)	32.7 (1.5)
	glass	6	79.2 (0.3)	13.7 (0.2)	1.4 (0.1)	5.6 (0.1)	
75/30/4	plag	7	60.9 (0.5)	24.6 (0.4)	6.9 (0.4)	7.5 (0.3)	33.9 (2.0)
	glass	8	80.0 (0.5)	13.3 (0.4)	1.1 (0.1)	5.6 (0.1)	
75/30/7	plag	7	61.3 (0.4)	24.4 (0.2)	6.7 (0.4)	7.5 (0.2)	33.0 (1.6)
	glass	8	82.3 (0.4)	11.9 (0.2)	0.8 (0.1)	5.0 (0.3)	
75/30/17	plag	7	61.8 (1.3)	24.1 (0.9)	6.7 (0.5)	7.4 (0.2)	33.3 (1.8)
	glass	6	81.8 (0.4)	12.1 (0.4)	0.8 (0.2)	5.3 (0.1)	
50/1200/0	glass	7	78.3 (0.1)	14.1 (0.2)	1.8 (0.1)	5.9 (0.1)	
50/1200/0-25	plag	n.d.	n.d.	n.d.	n.d.	n.d.	n.d.
	glass	7	78.3 (0.2)	14.3 (0.1)	1.8 (0.1)	5.6 (0.2)	
50/1200/1	plag	5	63.6 (0.9)	22.9 (0.5)	6.2 (0.3)	7.3 (0.3)	32.1 (1.3)
	glass	6	78.3 (0.2)	14.3 (0.1)	1.8 (0.1)	5.6 (0.2)	
50/1200/2	plag	7	63.0 (0.6)	23.5 (0.3)	6.2 (0.2)	7.3 (0.3)	32.0 (1.2)
	glass	9	78.6 (0.4)	14.2 (0.3)	1.7 (0.1)	5.5 (0.5)	
50/1200/5	plag	8	62.9 (1.2)	21.0 (0.6)	5.4 (0.4)	7.9 (0.3)	27.6 (1.4)
	glass*	1	81.4	11.9	0.7	5.9	

(continued)

Table 3: Continued

Run no. ¹	Phase ²	n^3	SiO ₂ ⁴	Al ₂ O ₃ ⁴	CaO ⁴	Na ₂ O ⁴	An (mol %) ⁵
50/1200/17	plag	7	62.6 (0.5)	23.6 (0.3)	5.6 (0.4)	8.2 (0.2)	27.4 (1.8)
	glass*	7	82.6 (0.5)	11.7 (0.9)	0.6 (0.3)	5.1 (0.3)	
50/150/0	glass	16	78.4 (0.3)	13.9 (0.2)	1.8 (0.1)	5.9 (0.2)	
50/150/2	plag	7	63.2 (1.1)	23.2 (0.8)	6.1 (0.4)	7.5 (0.2)	31.0 (1.6)
	glass	7	78.6 (0.3)	14.3 (0.2)	1.7 (0.1)	5.5 (0.4)	
50/150/4	plag	8	61.3 (0.8)	23.4 (0.5)	5.6 (0.4)	8.0 (0.2)	27.7 (1.8)
	glass*	7	81.6 (0.8)	12.6 (0.6)	0.7 (0.1)	5.1 (0.3)	
50/150/17	plag	7	63.0 (0.4)	23.3 (0.4)	5.1 (0.2)	8.6 (0.2)	24.6 (1.1)
	glass*	8	82.9 (0.3)	11.6 (0.3)	0.4 (0.1)	5.1 (0.1)	
50/30/0	glass	20	78.5 (0.2)	14.0 (0.2)	1.8 (0.1)	5.8 (0.2)	
50/30/2	plag	7	63.2 (0.8)	23.2 (0.5)	6.0 (0.3)	7.6 (0.1)	30.5 (1.2)
	glass	6	78.9 (0.6)	14.1 (0.4)	1.4 (0.1)	5.5 (0.2)	
50/30/4	plag	5	63.6 (0.5)	22.9 (0.3)	5.6 (0.2)	7.9 (0.3)	28.0 (1.1)
	glass*	6	79.4 (0.3)	14.0 (0.2)	1.0 (0.1)	5.7 (0.1)	
50/30/7	plag	7	62.9 (0.6)	23.5 (0.4)	5.8 (0.4)	7.8 (0.2)	28.9 (1.7)
	glass*	6	81.2 (0.6)	12.7 (0.5)	0.7 (0.1)	5.4 (0.1)	
50/30/17	plag	6	63.2 (0.9)	23.4 (0.6)	5.3 (0.3)	8.0 (0.2)	26.6 (1.6)
	glass*	6	82.8 (0.4)	11.7 (0.2)	0.4 (0.1)	5.0 (0.2)	
25/1200/2	plag	n.d.	n.d.	n.d.	n.d.	n.d.	n.d.
	glass*	5	78.5 (0.2)	14.2 (0.1)	1.6 (0.1)	5.7 (0.2)	

¹Run number as in Tables 1 and 2.

²Phase is either plagioclase (plag) or residual glass (glass); * marks the presence of a silica phase.

³ n gives the number of analyses.

⁴Contents of SiO₂, Al₂O₃, CaO, and Na₂O in wt %, with statistical error in parentheses; glasses recalculated on anhydrous basis.

⁵Anorthite content of the plagioclase in mol %, with statistical error in parentheses.

n.d., not determined.

early time evolution of Φ actually follows an exponential law (Fig. 4h). The data point obtained at $P_f=75$ MPa and 1 day confirms such a trend (Fig. 4e). However, because we lack a complete dataset at time <2 days, we will not further consider this early time evolution of Φ . The fitting parameters of the square-root laws for N_a , Φ , and $L/2$, and the time intercept with the plateau value are reported in Table 4.

DISCUSSION

Equilibrium degassing

The plagioclase stability curve used to constrain ΔT_{eff} entirely depends on the assumption that water exsolution keeps up with decompression through time (equilibrium degassing). Thus, it is crucial to verify this assumption, particularly in the light of the fast decompression rates used in this study. In particular, a decompression rate of 1200 MPa h⁻¹ stands on the side of equilibrium melt water exsolution after Martel & Schmidt (2003), close to equilibrium degassing after Rutherford (2008)

(i.e. ~ 900 MPa h⁻¹), and on the non-equilibrium degassing side after Mangan & Sisson (2000).

First, we assessed whether melt–bubble equilibrium was maintained with respect to water distribution on the time-scale of our experimental decompressions, by measuring glass water contents by the EMP by-difference method (using hydrated glass standards; see the section ‘Experimental and analytical methods’). To compare our measurements with water solubility models in rhyolites, we first analyzed the HTND glass hydrated at 200 MPa and 875°C (run 200B), giving 6.7 ± 0.3 wt % H₂O, whereas the model of Newman & Lowenstern (2002) predicts 5.8 wt %. This suggests a potential ~ 1 wt % overestimation in our measurements. Water measurements in glass samples quenched just after decompression to $P_f=50$ MPa (time = 0 at P_f) suggest 3.5 ± 0.5 , 3.2 ± 0.3 , and 3.2 ± 0.5 wt % for decompression rates of 1200, 150, and 30 MPa h⁻¹, respectively (Table 5). These results are 0.7–1.0 wt % higher than the value of 2.5 ± 0.2 wt % calculated at 875°C and 50 MPa after Newman & Lowenstern (2002), which agrees with the overestimation value

Table 4: Parameters of the equations fitting the time-dependent evolution curves of plagioclase number density, content, and size

Data points*			Square root of time [†]		
			f(x) = a√(x - t _n)		Intercept
P _f (MPa)	Parameter	ΔP/Δt (MPa h ⁻¹)	t _n (day)	a	i ± 0.5 (day)
100	N _a	1200	1.5	0.53	2
		150	1.5	117.20	5
		30	1.5	71.70	4
	Φ	1200	1.5	0.53	2
		150	1.5	4.90	5
		30	1.5	5.41	5
	L/2	1200	1.5	52.07	4
		150	1.5	70.32	4
		30	1.5	72.15	4
75	N _a	1200	0.7	63.14	5
		150	0.7	128.98	7
		30	0.7	196.68	7
	Φ	1200	1.5	5.51	9
		150	1.5	7.75	8
		30	1.5	8.10	7
	L/2	1200	0.7	37.63	9
		150	0.7	26.98	8
		30	0.7	34.44	7
50	N _a	1200	0.2	433.81	6
		150	0.2	445.78	4
		30	0.2	634.16	4
	Φ	1200	1.0	8.43	7
		150	1.0	11.13	7
		30	1.0	10.14	7
	L/2	1200	0.2	52.31	3
		150	0.2	26.05	4
		30	0.2	29.17	4

*From Fig. 4.

[†]Fitting equation, defined with constant a and variable x = time (in days), with boundary conditions of t_n (nucleation time) and i [intercept between $f(x)$ and the plateau value]. It should be noted that at $P_f = 75$ and 50 MPa, t_n for Φ is different from that for N_a or $L/2$ owing to the exponential starting curve (Fig. 4e-h).

previously observed between measurements and calculation. Additionally, these water measurements are comparable, within error, with those for samples annealed at $P_f = 50$ MPa for 2 or 17 days (2.6–3.5 wt % H₂O; Table 5), for which the long durations are in favor of equilibrium degassing. Thus, we infer that degassing reached equilibrium during decompression duration.

We calculated the characteristic time, t_c , required for water to diffuse in the melt until equilibrium, following the equation given by Navon *et al.* (1998):

$$t_c = \delta^2 / (4 \times D_w)$$

where δ is the average half-length between two bubbles and D_w is the water diffusion coefficient in the melt. Taking δ as the maximum value of 100 μm retrieved from run 50/1200/0 (Fig. 6b) and $D_w = 7.4 \mu\text{m}^2 \text{s}^{-1}$ calculated after Zhang & Behrens (2000) for a melt water content of 2.5 wt % yields a maximum t_c of ~ 5.5 min. This is shorter than the decompression duration of 7.5 min corresponding to the fastest decompression rate of 1200 MPa h⁻¹, which may also validate equilibrium water degassing.

In parallel, we compared the porosity of the sample quenched just after decompression to $P_f = 50$ MPa at a rate of 1200 MPa h⁻¹ (Fig. 6b) with the porosity calculated for equilibrium degassing following the equation of Jaupart & Tait (1990). We measured a porosity of $44 \pm 3\%$ and the calculation gives $42 \pm 3\%$ [water solubility at 200 and 50 MPa of 5.8 and 2.5 wt %, respectively (Newman & Lowenstern, 2002); melt density of 2200 kg m⁻³ (Knoche *et al.*, 1995) and gas density at 50 MPa and 875°C of 99 kg m⁻³ (Saul & Wagner, 1989)]. Again, the comparison validates equilibrium degassing. The samples that were quenched just after decompression to 50 MPa at rates of 150 and 30 MPa h⁻¹ (decompression duration of 1 and 5 h, respectively; Fig. 6c) show lower bubble contents (37 ± 3 and $36 \pm 3\%$, respectively; Table 5) than that expected at equilibrium degassing, probably resulting from gas escape during decompression, either by gas channeling or by direct diffusive water loss towards the sample outer rims. After anneal durations of 17 days, the samples show porosities below 10% (Fig. 6d).

Parameters controlling plagioclase crystallization

ΔT_{eff} (or P_f)

Nucleation lag. ΔT_{eff} shows a significant effect on the delay of plagioclase nucleation, with a lag decreasing from 2–3 days for $\Delta T_{\text{eff}} < 25^\circ\text{C}$ to less than 6 h for $\Delta T_{\text{eff}} = 110^\circ\text{C}$ (Fig. 7). Couch *et al.* (2003) suggested nucleation lags of 4–8 h for $\Delta T_{\text{eff}} \sim 38^\circ\text{C}$, but their starting melt contains 1–2% plagioclase, so that ΔT_{eff} from the liquidus must be higher than 38°C (we actually calculated $\Delta T_{\text{eff}} \sim 80^\circ\text{C}$; see the section on ‘Crystallization regime’ below). In our experiments, for which degassing equilibrates before crystallization pressure, the nucleation lag is interpreted as the time required for the crystal nucleus to reach critical size. For small undercooling, the critical size is large so that an atom cluster requires a relatively long period of time to reach the required size. In contrast, for large undercooling, the critical size of the crystal nucleus is

Table 5: Water degassing conditions

Run*	P_f (MPa)	Δt (min)	Time at P_f (day)	Melt H ₂ O content†		Porosity		
				n	H ₂ O (wt %)	N_{bubble} (mm ⁻²)	P_{\ddagger}^{\dagger} (%)	P_{calc}^{\S} (%)
200B	200	0	6	31	6.7 (0.3)	21	1	0
50/1200/0	50	7.5	0	12	3.5 (0.5)	396	44 (3)	42 (3)
50/1200/2	50	7.5	2	7	2.6 (0.4)	n.d.	n.d.	42 (3)
50/1200/17	50	7.5	17	7	3.2 (0.3)	44	6 (3)	42 (3)
50/150/0	50	60	0	8	3.2 (0.3)	295	37 (3)	42 (3)
50/150/2	50	60	2	8	3.5 (0.2)	n.d.	n.d.	42 (3)
50/150/17	50	60	17	7	3.2 (0.2)	n.d.	n.d.	42 (3)
50/30/0	50	300	0	13	3.2 (0.3)	192	36 (3)	42 (3)
50/30/2	50	300	2	19	3.2 (0.3)	n.d.	n.d.	42 (3)
50/30/17	50	300	17	5	3.1 (0.3)	81	4 (3)	42 (3)

*Run conditions as in Tables 1 and 2.

†H₂O content determined by the EMP by-difference method (Devine *et al.*, 1995), with statistical error in bracket; n is the number of analyses.

‡Porosity measured by image analysis.

§Porosity calculated at equilibrium after Jaupart & Tait (1990) (see text).

Statistical error is given in parentheses. n.d., not determined.

small and atom clusters require shorter time to form a nucleus (Gibb, 1974).

N_a , Φ , and $L/2$. With increasing ΔT_{eff} , the maximum N_a values increase following power laws (Fig. 8a), reflecting the progressive dominance of the nucleation process as crystallization pressure decreases. The maximum Φ values drastically increases from $\Delta T_{\text{eff}} \sim 55^\circ\text{C}$ to $\sim 110^\circ\text{C}$ to a value of 20–25% at $\Delta T_{\text{eff}} \sim 110^\circ\text{C}$ (Fig. 8b) that must be close to equilibrium, as expected from phase equilibrium data for rhyolitic melts (water-saturated conditions; e.g. Couch *et al.*, 2003; Martel, 2012).

Composition. The An decrease of the plagioclase equilibrium composition, from An₄₃ at $P_f = 160$ MPa to An_{24–28} at $P_f = 50$ MPa (Fig. 5a, c and e; Table 3), is in agreement with the trend expected from phase equilibrium data for rhyolitic melts (water-saturated conditions; e.g. Couch *et al.*, 2003; Martel, 2012).

Morphology. Plagioclase crystal morphology depends markedly on ΔT_{eff} (Fig. 8). For $\Delta T_{\text{eff}} < 40^\circ\text{C}$, plagioclase crystals show compact tabular or rectangular habits, which is in good agreement with the results of either cooling-induced plagioclase crystallization from plagioclase melts (Lofgren, 1974; Muncill & Lasaga, 1987, 1988) or decompression-induced crystallization (single-step decompression experiments, SDE; Hammer & Rutherford, 2002; Couch *et al.*, 2003). We observed skeletal or hollow morphologies for $4^\circ\text{C} < \Delta T_{\text{eff}} < \sim 150^\circ\text{C}$ (at least $> 110^\circ\text{C}$), as either rectangular prisms for $40^\circ\text{C} < \Delta T_{\text{eff}} < 80^\circ\text{C}$ or acicular habits for $80^\circ\text{C} < \Delta T_{\text{eff}} < \sim 150^\circ\text{C}$. This ΔT_{eff} range is significantly higher than the range of 40–60°C

reported for skeletal habits in cooling-induced plagioclase crystallization (Lofgren, 1974; Muncill & Lasaga, 1987, 1988). Nevertheless, it agrees with crystallization in SDE (Hammer & Rutherford, 2002; Couch *et al.*, 2003) and in phase equilibrium experiments on water-saturated rhyolitic melts (Martel, 2012). Similarly, we find dendritic crystal shapes for $\Delta T_{\text{eff}} > \sim 150^\circ\text{C}$, which is a far higher value than the range of 60–80°C reported for cooling-induced crystallization, but agrees with crystallization in SDE or phase equilibria experiments. Therefore, our results confirm that plagioclase morphologies resulting from crystallization driven by cooling (ΔT) are not comparable with those resulting from isothermal melt dehydration or decompression (ΔT_{eff}). However, the various studies that dealt with plagioclase crystallization driven by melt dehydration all agreed on the relationship between ΔT_{eff} and crystal morphology (Hammer & Rutherford, 2002; Couch *et al.*, 2003; Martel, 2012).

Plagioclase Ostwald ripening

In most samples, the time evolution of N_a at P_f rapidly reaches a steady state. However, the samples decompressed at 30 MPa h⁻¹ to $P_f = 75$ MPa (Fig. 4d) and the samples decompressed at 30 and 1200 MPa h⁻¹ to $P_f = 50$ MPa (Fig. 4g) show a decrease of N_a after having reached a maximum value.

One may invoke a process of Ostwald ripening, by which large crystals grow with time at the expense of smaller ones that dissolve, to reduce the excess energy associated with solid–liquid interfaces. During Ostwald

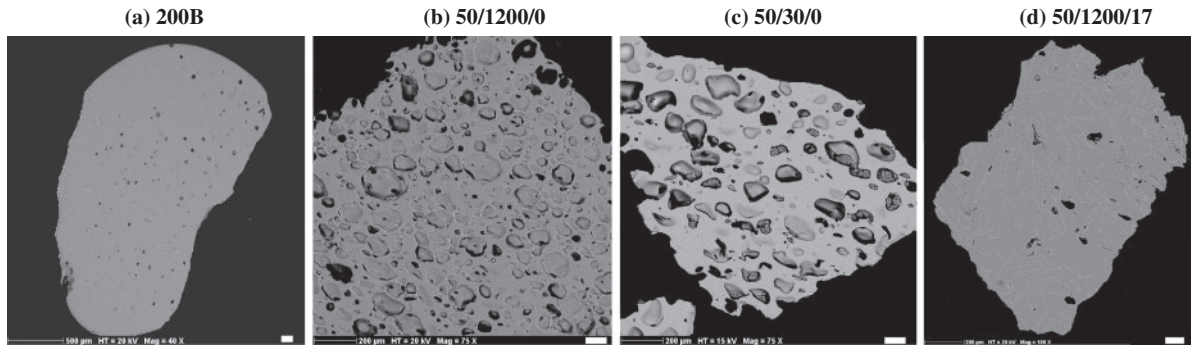


Fig. 6. Sample porosity for the starting sample hydrated at 875 °C and 200 MPa for 6 days (a), samples quenched at $P_f = 50$ MPa just after decompression (time = 0) at a rate of 1200 MPa h⁻¹ (b) and 30 MPa h⁻¹ (c), and the sample quenched after 17 days at $P_f = 50$ MPa (d). The white scale bars represent 100 μm.

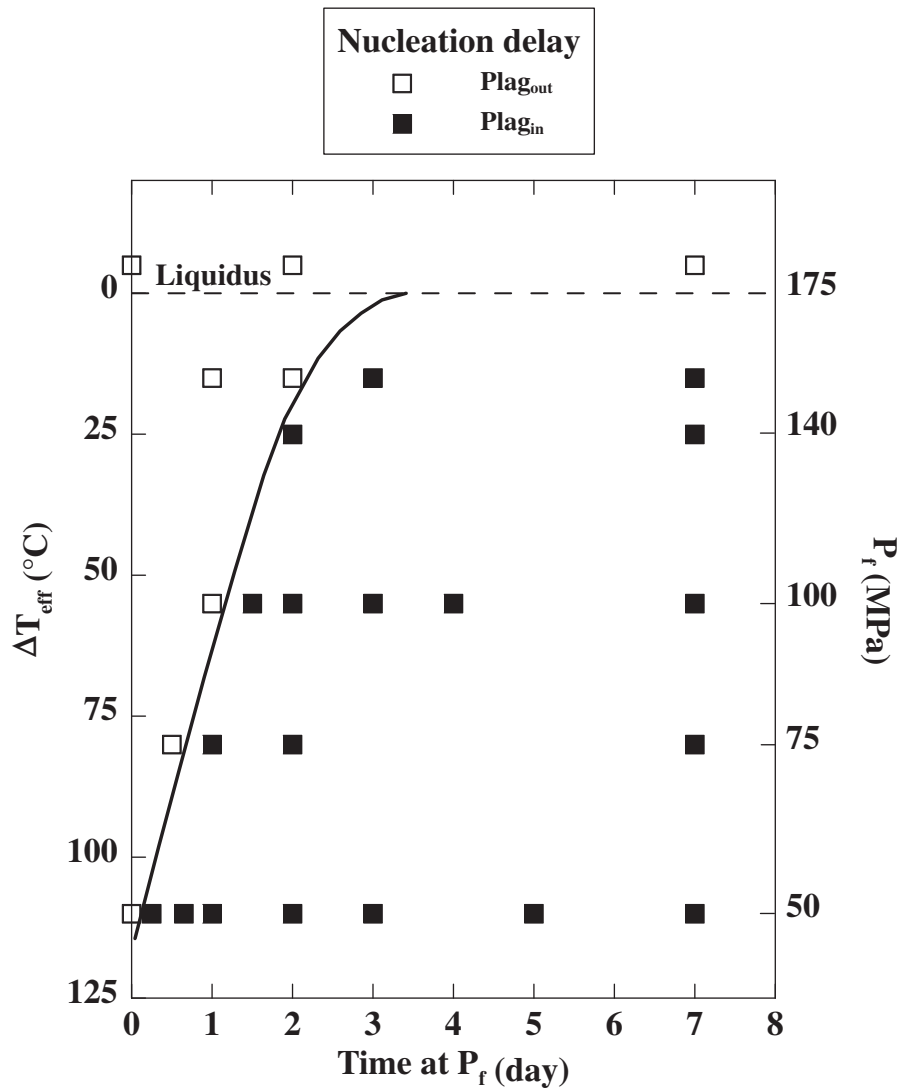


Fig. 7. Plagioclase nucleation delay plotted from the crystal-bearing and crystal-free samples as a function of ΔT_{eff} ($\Delta P/\Delta t = 1200$ MPa h⁻¹).

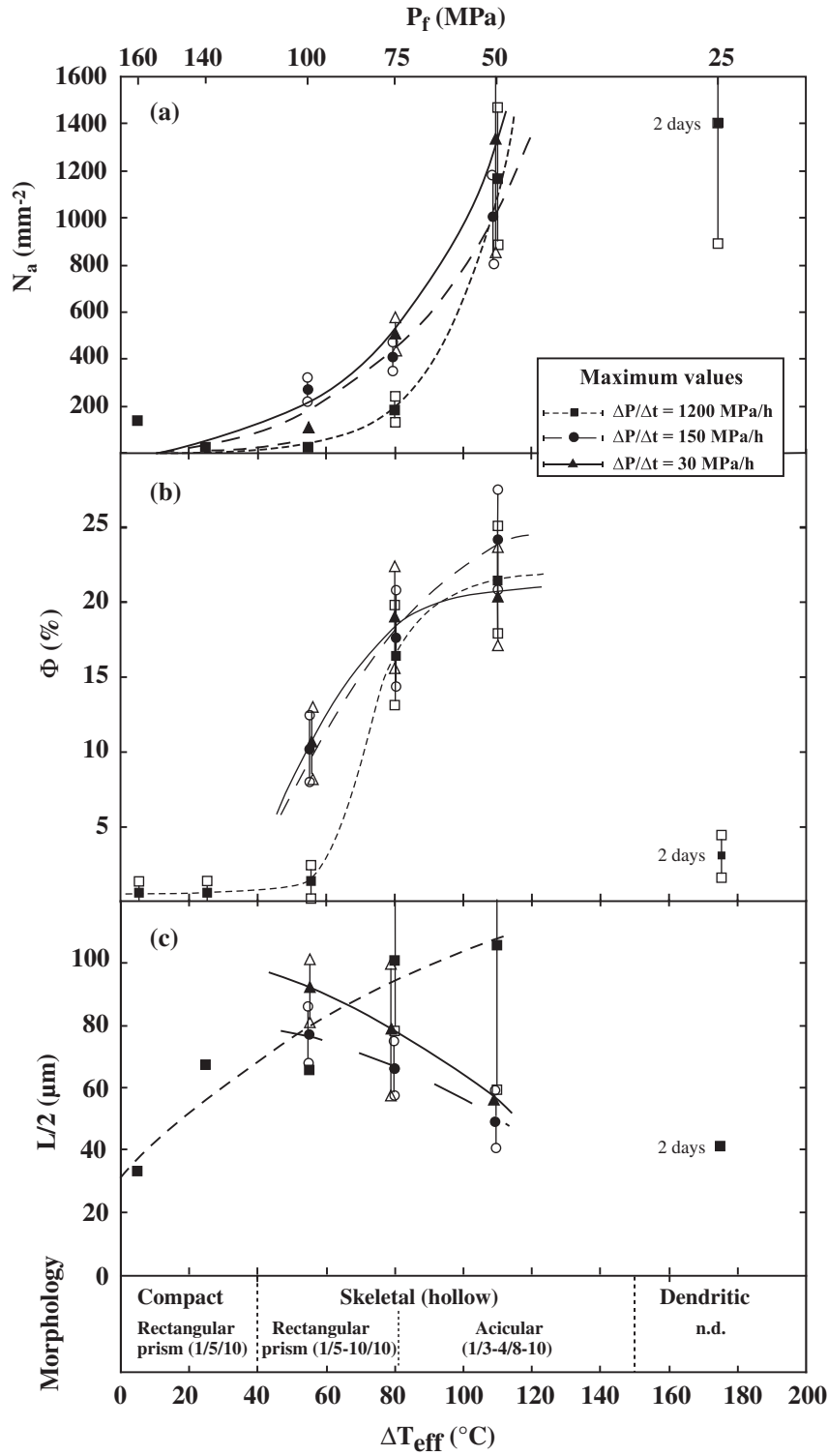


Fig. 8. Evolution of N_a (a), Φ (b), and $L/2$ (c) as a function of ΔT_{eff} and $\Delta P/\Delta t$. Data points are the maximum values given in Fig. 4.

ripening, the decrease of N_a is commonly accompanied by an increase of crystal size, but Cabane *et al.* (2005) observed that, for Ostwald ripening of plagioclase crystals in silicate melts, crystal size is rapidly buffered, an observation that is consistent with our experiments (Fig. 4f and i).

Ostwald ripening in silicate melts has mostly been interpreted as being controlled by a surface nucleation process at the crystal–liquid interface (Cabane *et al.*, 2005). We propose that the occurrence of Ostwald ripening results from the high N_a generated at $P_f \leq 75$ MPa. For example, at $P_f = 50$ MPa, there must be a critical N_a around 1000 mm^{-2} above which Ostwald ripening is favored by short crystalline inter-distances.

Pre-crystallization decompression

The evolution of N_a , Φ , $L/2$, and composition with ΔT_{eff} mostly follow the same trends, within error, as a function of $\Delta P/\Delta t$. However, in detail, there is a tendency for the samples decompressed at a rate of 1200 MPa h^{-1} to show lower N_a and lower Φ than the samples decompressed at rates of 30 and 150 MPa h^{-1} (Fig. 8a and b). Φ is particularly low at $P_f = 100$ MPa, resulting in residual glasses that are clearly depleted in SiO_2 (Fig. 5b). The 1200 MPa h^{-1} series display a positive correlation between $L/2$ and ΔT_{eff} , with a maximum value expected at $\Delta T_{\text{eff}} \geq 110^\circ\text{C}$. In contrast, the 30 and 150 MPa h^{-1} series have a maximum $L/2$ for $\Delta T_{\text{eff}} \leq 55^\circ\text{C}$ (Fig. 8c). Overall, low N_a , low Φ , and the dominance of growth regime up to high ΔT_{eff} could reveal nucleation difficulties at small ΔT_{eff} in the samples decompressed at 1200 MPa h^{-1} .

Previous studies have reported the absence of a clear relationship between pre-crystallization decompression rate and plagioclase composition (Castro & Gardner, 2008; Brugger & Hammer, 2010), a result that is also consistent with our data (Fig. 5). Nevertheless, insignificant or positive correlations between N_a and pre-crystallization decompression rate have been suggested (Couch *et al.*, 2003; Martel & Schmidt, 2003; Martel, 2012). In particular, the experiments performed by Martel (2012), which have many similarities to the present ones (same experimental device, crystal-free and water-saturated starting samples, similar run temperatures and pressures, similar decompression rates, and plagioclase as the major crystallizing phase), reported a positive correlation between N_a and pre-crystallization decompression rate. The primary difference between these observations and our experiments is melt composition. Specifically, compared with the four-element-bearing HTND, the synthetic rhyolite of Martel (2012), as well as that of Couch *et al.* (2003) and Martel & Schmidt (2003), contains five additional elements (Fe, Mg, Mn, K, Ti) that could influence melt–crystal surface tensions and result in nucleation behaviors different from those observed in compositionally more simple systems (Müller *et al.*, 1992). However, we do not see crystallization differences between the samples decompressed

at rates of 30 and 150 MPa h^{-1} , suggesting that only the 1200 MPa h^{-1} series behave differently. Therefore, we speculate that such a high decompression rate generates atomic structural arrangements in the melt that may be different from (less relaxed than?) those in melts decompressed more slowly, which may further modify the solid–liquid interfaces and nucleation conditions.

Crystallization kinetics

Rates of nucleation (I) and growth (U) were obtained from time-derivatives of the square-root functions fitting the N_a and $L/2$ data, respectively, the equations for which are given in Table 4. In comparison with the crystallization rates commonly determined by integrating between two data points over a given period of time (e.g. Hammer & Rutherford, 2002; Couch *et al.*, 2003; Brugger & Hammer, 2010), function derivatives have the advantages of (1) providing rates at any time and (2) being particularly well suited to rate modelling issues.

Effect of ΔT_{eff} on nucleation rate (I)

The time evolution of I passes through a maximum value, I_{max} , at the very beginning of nucleation and drastically decreases with time (Fig. 9a–c). I_{max} increases from $\sim 10^{-3} \text{ mm}^{-2} \text{ s}^{-1}$ for $\Delta T_{\text{eff}} \sim 55^\circ\text{C}$ (except in the 1200 MPa h^{-1} series, which was subject to nucleation difficulty) to $\sim 10^{-2} \text{ mm}^{-2} \text{ s}^{-1}$ for $\Delta T_{\text{eff}} \sim 110^\circ\text{C}$ (Table 6), highlighting the progressive domination of the nucleation process towards high ΔT_{eff} . This positive correlation between I_{max} and ΔT_{eff} is in agreement with the conclusions of Fenn (1977) and Swanson (1977), who documented an increase in alkali-feldspar nucleation rate with decreasing water content in granitic systems (i.e. decreasing P_f for water-saturated melts). Our results are also in agreement with the decompression-induced incremental I_{max} reported by Couch *et al.* (2003) (Fig. 10a).

Nucleation delays and rates reported in Fig. 9 suggest that magma decompressed to low pressure (high ΔT_{eff}) nucleates microlites early (within the first hour) and massively, thus drastically changing the physicochemical and rheological properties of the magma. In contrast, a melt rapidly decompressed to a relatively high final pressure (low ΔT_{eff}) only crystallizes a few microlites after 1–2 days, which have little effect on magma rheology. These few microlites, however, may act as preferential sites for future growth-dominated crystallization at lower pressures.

Effect of ΔT_{eff} on growth rate (U)

Similarly to I , the time evolution of U passes through a sharp maximum, U_{max} , and further decreases with time (Fig. 9d–f). In contrast to I_{max} , U_{max} decreases with ΔT_{eff} , from $\sim 10^{-6} \text{ mm s}^{-1}$ for $\Delta T_{\text{eff}} \sim 55^\circ\text{C}$ to $\sim 5 \times 10^{-6} \text{ mm s}^{-1}$ for $\Delta T_{\text{eff}} \sim 110^\circ\text{C}$ (with the exception of the 1200 MPa h^{-1} series in which crystal sizes were particularly difficult to

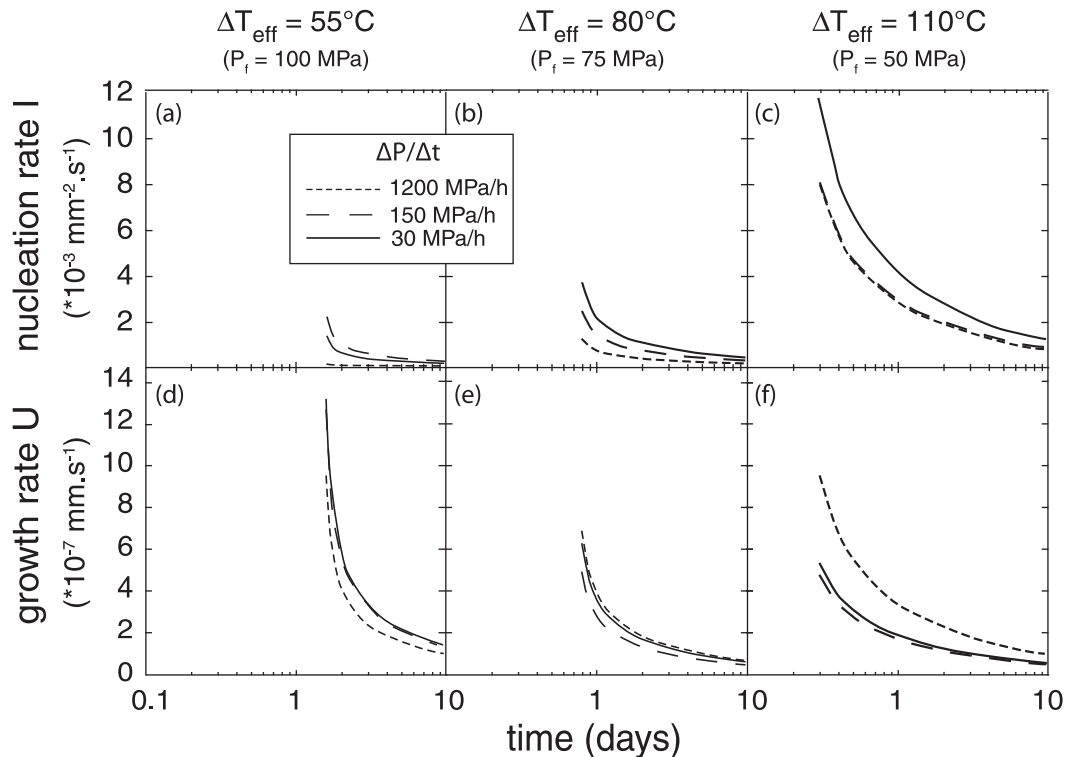


Fig. 9. Plagioclase nucleation rate, I (a–c) and growth rate, U (d–f), calculated from the time-derivatives of the N_a and $L/2$ fit functions given in Table 4, respectively. The I and U dependence on crystallization duration at P_i and ΔT_{eff} should be noted.

Table 6: Maximum nucleation and growth rates

ΔT_{eff} ($^\circ\text{C}$)	$I_{\text{max}} \times 10^{-3} \text{ (mm}^{-2} \text{ s}^{-1})^*$			$U_{\text{max}} \times 10^{-7} \text{ (mm s}^{-1})^*$		
	1200†	150†	30†	1200†	150†	30†
55	0.01	2.1	1.3	9.5	12.9	13.2
80	1.2	2.5	3.6	6.9	4.9	6.3
110	8.2	7.9	11.6	9.6	4.8	5.3

*Maximum nucleation and growth rates deduced from the derivatives of the square-root functions for N_a and $L/2$, respectively, given in Table 4.

†Pre-crystallization decompression rates in MPa h^{-1} .

define, potentially leading to large errors on U). Our U_{max} values are 1–4 log units higher than the range of 10^{-7} – $10^{-10} \text{ mm s}^{-1}$ previously estimated for groundmass plagioclase growth rates in intermediate to silicic magmas (Cashman, 1988, 1992; Geschwind & Rutherford, 1995; Gardner *et al.*, 1998; Hammer *et al.*, 1999; Cashman & Blundy, 2000; D’Orlando *et al.*, 2005; Brugger & Hammer, 2010). The discrepancy mainly results from the fact that we calculated growth rates from the 10 longest crystals, whereas previous researchers mostly calculated mean values on the whole crystal population. Nevertheless,

our U_{max} values are of the order of magnitude of those determined by Hammer & Rutherford (2002) and Couch *et al.* (2003), both groups of researchers having calculated time-integrated U_{max} from the 10 longest crystals. However, both studies reported U_{max} at $\Delta T_{\text{eff}} > 55^\circ\text{C}$, whereas our curves would suggest U_{max} at $\Delta T_{\text{eff}} < 55^\circ\text{C}$ (Fig. 10b). The fact that the kinetic regime dominated by growth is extended to the small ΔT_{eff} in our study may be related to the crystal-free nature of our starting glasses, for which growth is precisely detected. In contrast, the initial plagioclase crystals in the starting samples of Hammer & Rutherford (2002) and Couch *et al.* (2003) may take part in the crystallization by crystal overgrowth, which is not further counted as such (as only newly formed crystals are taken into account in these studies).

Crystallization regime

Plotting the experimentally determined N_a vs Φ , together with data from the single-step decompression experiments of Couch *et al.* (2003), Brugger & Hammer (2010) (their ‘anneal’ runs have been rapidly decompressed from initial pressure) and Martel (2012), defines an exponential correlation for ΔT_{eff} up to $\sim 200^\circ\text{C}$ (Fig. 11). For $\Delta T_{\text{eff}} > 200^\circ\text{C}$, the data show scatter in Φ , from 10–30% (Martel, 2012) to 45–50% (Brugger & Hammer, 2010). This shift at low crystallization pressure may reflect

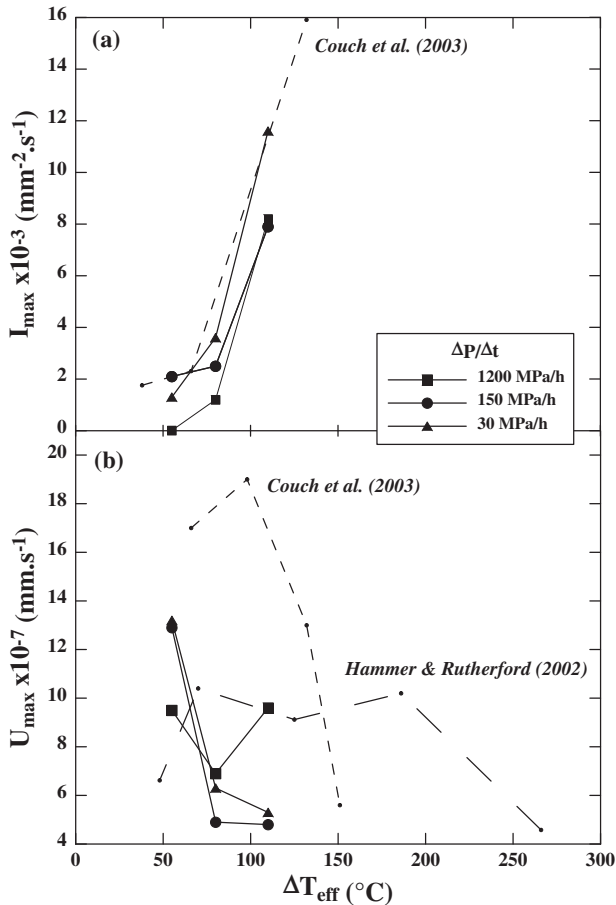


Fig. 10. Maximum rates of nucleation, I_{\max} (a) and growth, U_{\max} (b) as a function of ΔT_{eff} . For comparison, time-integrated I_{\max} and U_{\max} calculated for single-step decompressions followed by isobaric crystallization steps are reported from the literature (Hammer & Rutherford, 2002; Couch *et al.*, 2003, for a time interval of 1–4 h).

temperature and melt composition effects on crystallinity, as Brugger & Hammer (2010) performed experiments at 880°C starting with a normative-Qz₂₁ bulk sample, compared with 850°C and normative-Qz₄₃ composition used by Martel (2012).

Thus, provided temperature and composition (normative Qz content) are comparable with those reported here, evaluation of N_a , Φ , and crystal morphology from either experimental or natural samples provides a means to assess both ΔT_{eff} prevailing during isobaric crystallization and plagioclase liquidus temperature or pressure (Fig. 11).

For example, the plagioclase liquidus of the Aniakchak rhyodacite used in the decompression experiments of Brugger & Hammer (2010) has been determined from phase equilibrium experiments by Larsen (2006). Plotting N_a – Φ data from the Brugger & Hammer (2010) experiments at $P_f = 5, 26, 45,$ and 87 MPa suggests crystallization under $\Delta T_{\text{eff}} > 200, \sim 175, \sim 85,$ and $\sim 55^{\circ}\text{C}$, respectively

(Fig. 11). From magma temperature (880°C; Larsen, 2006) and ΔT_{eff} , we can deduce plagioclase liquidus temperatures of $> 1080, \sim 1055, \sim 965,$ and $\sim 935^{\circ}\text{C}$ at the respective P_f . Because the plagioclase liquidus curves are parallel in pressure–temperature space (water saturation; Fig. 2), extrapolation of these liquidus to $\Delta T_{\text{eff}} = 0^{\circ}\text{C}$ suggests a plagioclase liquidus pressure of ~ 150 MPa at 880°C. This finding compares well with the plagioclase liquidus pressure at 880°C determined by Larsen (2006), giving confidence in using ΔT_{eff} -constrained N_a – Φ plots to deduce plagioclase liquidus locations.

In the experiments of Couch *et al.* (2003) the plagioclase liquidus temperature of the Soufrière Hills interstitial rhyolitic melt is not precisely known because the pre-decompression starting melts already contain 1–2 vol. % plagioclase. Assuming that N_a compares with our crystal-free melts (or at least I_{\max} compare; Fig. 10a), we can propose plagioclase liquidus temperatures of $> 1075^{\circ}\text{C}$ at 50 MPa to $\sim 960^{\circ}\text{C}$ at 125 MPa, using our ΔT_{eff} -constrained N_a – Φ plot. Extrapolating these liquidus temperatures to $\Delta T_{\text{eff}} = 0^{\circ}\text{C}$ yields a plagioclase saturation pressure of ~ 210 MPa at 875°C [which approximately leads to adding $\sim 40^{\circ}\text{C}$ to the ΔT_{eff} reported by Couch *et al.* (2003)].

APPLICABILITY TO VOLCANIC SYSTEMS

The empirically derived nucleation and growth laws provide time information on the decompression-induced isobaric crystallization of plagioclase from a silica-rich melt ($\text{SiO}_2 > 75$ wt %). In particular, we provide plagioclase nucleation lags (Fig. 7) and rates of nucleation and growth as a function of ΔT_{eff} (Fig. 10). In turn, these results represent experimental clues to back-track ΔT_{eff} conditions and plagioclase liquidus temperatures prevailing during crystallization of natural plagioclase microlites from rhyolitic melts (Fig. 11).

First, because recent experiments have evidenced a significant influence of the presence of initial crystals in the starting melt on further decompression-induced crystallization (particularly on N_a ; Martel, 2012), the application of pure starting melts may be restricted to aphyric or phenocryst-poor rhyolites, typically obsidians or rhyolites in which microlites could nucleate homogeneously between distant phenocrysts. Second, the simulation of a rapid decompression that triggers isobaric crystallization may not represent the most common mode of ascent and crystallization of natural silicic magmas. Indeed, magmas from dome-related eruptions typically ascend slowly, giving time for syn-decompression microlite crystallization controlled by transient (increasing) ΔT_{eff} . Nevertheless, some obsidians and rhyolites do ascend rapidly, crystallizing microlites during a stall at shallow depth (Castro &

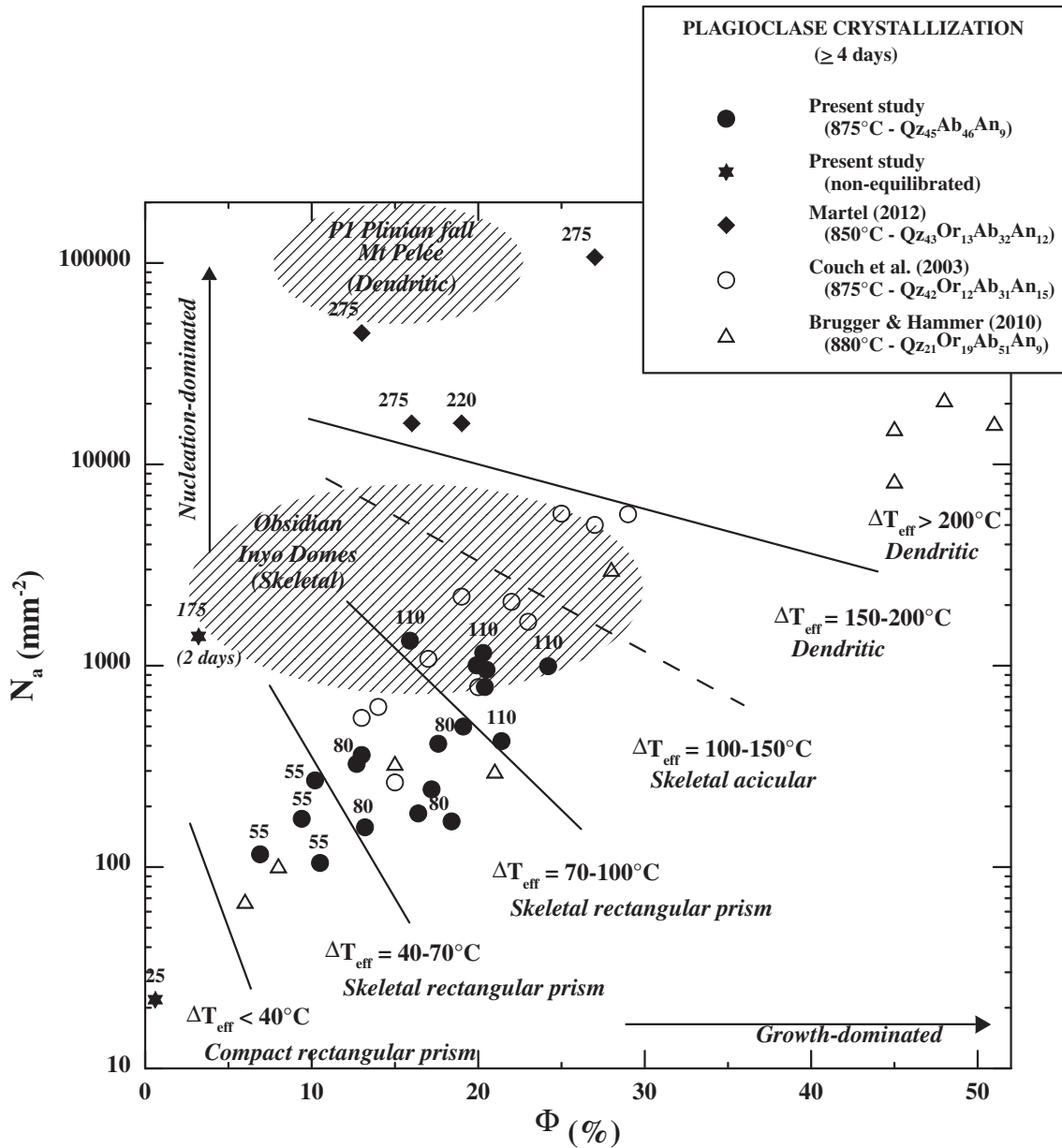


Fig. 11. Textural evolution of plagioclase as a function of ΔT_{eff} (for crystallization durations ≥ 4 days). Filled symbols represent crystallization from pure melts, whereas open symbols characterize pre-decompression melts containing 1–2% plagioclase. Point labels give ΔT_{eff} (in $^{\circ}\text{C}$), delimiting areas of iso- ΔT_{eff} for which crystal morphology is compact, skeletal, or dendritic. Filled circles are from Table 2, without the data at $\Delta P/\Delta t = 1200 \text{ MPa h}^{-1}$ and $\Delta T_{\text{eff}} = 55^{\circ}\text{C}$, for which crystallization difficulties have been reported. The data at $\Delta T_{\text{eff}} = 25^{\circ}\text{C}$ ($P_f = 140 \text{ MPa}$, 7 days) have been added as a non-equilibrated sample. Fields with diagonal line shading indicate natural microlite data from the Pl Plinian eruption of Mt Pelee (Martel & Poussineau, 2007) and obsidians from Inyo Domes (Castro & Mercer, 2004; Castro & Gardner, 2008).

Dingwell, 2009; Martel, 2012). Microlite number density in pyroclasts from pulsed magma ascents [e.g. Mount St Helens summer 1980 eruptions (Cashman & McConnell, 2005) or Soufrière Hills, Montserrat, vulcanian eruptions (Druitt *et al.*, 2002)] could also be interpreted in terms of the ΔT_{eff} prevailing during nucleation, provided evidence exists that N_a represents a single nucleation event (occurring at high pressure and small ΔT_{eff}) with further syn-

decompression crystallization occurring as growth around these early formed nuclei.

The full applicability of the present experimental data to various volcanic settings would require (1) more experimental data in more silica-poor liquids (typically 70–72 wt % SiO_2) and (2) further investigations of the microlite characteristics in phenocryst-poor rhyolites. At Inyo domes, California, rhyolitic obsidians display tabular to skeletal

plagioclase microlites with N_a from 10^3 to 10^4 mm⁻² and Φ from 2 to 30% (Castro & Mercer, 2004; Castro & Gardner, 2008). Although requiring further refinement of the natural microlite characteristics, the N_a - Φ values from Inyo Domes are compatible with the experimental data, suggesting possible rapid ascent of the obsidian magma followed by a stall and crystallization under ΔT_{eff} of 100–150°C (Fig. 11). Similarly, a detailed study of the microlite characteristics reported in the rhyolitic obsidians from Chaitén volcano, Chile, would potentially be relevant to retrieve ΔT_{eff} , as these magmas ascended very rapidly (Castro & Dingwell, 2009). At Mt Pelée, Martinique, the microlite-bearing pumices from the Plinian fallout (although containing ~40 vol. % of phenocrysts; Martel & Poussineau, 2007) show N_a , Φ , and microlite morphologies (dendritic) that are compatible with very low-pressure nucleation under $\Delta T_{\text{eff}} > 200^\circ\text{C}$ (Fig. 11).

ACKNOWLEDGEMENTS

We would like to gratefully thank Rémi Champallier, Didier Bellenoue, Philippe Teulat, and Esteban Le Moing for technical assistance with the pressure vessels, Olivier Rouer and Ida Di Carlo for technical assistance with SEM and EMP, Emmanuel Le Trong for helping to fit the data, and Laura Martel and Mathieu Allix for TEM analyses. We also thank Jessica Larsen, Thomas Shea, Don Dingwell, and Malcolm Rutherford for their very constructive reviews of the paper.

FUNDING

This work is part of E.M.'s PhD (MRT grant) and was funded by the Agence Nationale de la Recherche (Contract No. ANR-05-CATT-0004 to C.M.).

REFERENCES

- Behrens, H. (1995). Determination of water solubilities in high-viscosity melts: an experimental study on NaAlSi₃O₈ and KAlSi₃O₈ melts. *European Journal of Mineralogy* **7**, 905–920.
- Brandeis, G. & Jaupart, C. (1987). Crystal sizes in intrusions of different dimensions: Constraints on the cooling regime and the crystallization kinetics. In: Mysen, B. O. (ed.) *Magmatic Processes: Physicochemical Principles. Special Publication of the Geochemical Society* **1**, P307–318.
- Brugger, C. R. & Hammer, J. (2010). Crystallization kinetics in continuous decompression experiments: Implications for interpreting natural magma ascent processes. *Journal of Petrology* **51**, 1941–1965.
- Cabane, H., Laporte, D. & Provost, A. (2005). An experimental study of Ostwald ripening of olivine and plagioclase in silicate melts: implications for the growth and size of crystals in magmas. *Contributions to Mineralogy and Petrology* **150**, 37–53.
- Cashman, K. V. (1988). Crystallization of Mount St Helens 1980–1986 dacite: a quantitative textural approach. *Bulletin of Volcanology* **50**, 194–209.
- Cashman, K. V. (1992). Groundmass crystallization of Mount St Helens dacite, 1980–1986: a tool for interpreting shallow magmatic processes. *Contributions to Mineralogy and Petrology* **109**, 431–449.
- Cashman, K. V. & Blundy, J. (2000). Degassing and crystallization of ascending andesite and dacite. *Philosophical Transactions of the Royal Society of London, Series A* **358**, 1487–1513.
- Cashman, K. V. & McConnell, S. M. (2005). Multiple levels of magma storage during the 1980 summer eruptions of Mount St. Helens, WA. *Bulletin of Volcanology* **68**, 57–75.
- Castro, J. M. & Dingwell, D. B. (2009). Rapid ascent of rhyolitic magma at Chaitén volcano, Chile. *Nature* **461**, 780–783.
- Castro, J. M. & Gardner, J. E. (2008). Did magma ascent rate control the explosive–effusive transition at the Inyo volcanic chain, California? *Geology* **36**, 279–282.
- Castro, J. M. & Mercer, C. (2004). Microlite textures and volatile contents of obsidian from Inyo volcanic chain, California. *Geophysical Research Letters* **31**, L18605.
- Clarke, A. B., Stephens, S., Teasdale, R., Sparks, R. S. J. & Diller, K. (2007). Petrologic constraints on the decompression history of magma prior to Vulcanian explosions at the Soufrière Hills volcano, Montserrat. *Journal of Volcanology and Geothermal Research* **161**, 261–274.
- Couch, S., Sparks, R. S. J. & Carroll, M. R. (2003). The kinetics of degassing-induced crystallization at Soufrière Hills volcano, Montserrat. *Journal of Petrology* **44**, 1477–1502.
- Davis, M. J., Ihinger, P. D. & Lasaga, A. (1997). Influence of water on nucleation kinetics in silicate melt. *Journal of Non-Crystalline Solids* **219**, 62–69.
- Devine, J. D., Gardner, J. E., Brack, H. P., Layne, G. D. & Rutherford, M. J. (1995). Comparison of microanalytical methods for estimating H₂O contents of silicic volcanic glasses. *American Mineralogist* **80**, 319–328.
- Donaldson, C. H. (1979). An experimental investigation of the delay in nucleation of olivine in mafic magmas. *Contributions to Mineralogy and Petrology* **69**, 21–32.
- D’Orsiano, C., Poggianti, E., Bertagnini, A., Cioni, R., Landi, P., Polacci, M. & Rosi, M. (2005). Changes in eruptive style during the AD 1538 Monte Nuovo eruption (Phlegrean Fields, Italy): the role of syn-eruptive crystallization. *Bulletin of Volcanology* **67**, 601–621.
- Druitt, T. H., Young, S. R., Baptie, B. J., Bonadonna, C., Calder, E. S., Clarke, A. B., Cole, P. D., Harford, C. L., Herd, R. A., Lockett, R., Ryan, G. & Voight, B. (2002). Episodes of cyclic vulcanian explosive activity with fountain collapse at Soufrière Hills Volcano, Montserrat. In: Druitt, T. H. & Kokelaar, B. P. (eds) *The Eruption of Soufrière Hills Volcano, Montserrat, from 1995 to 1999. Geological Society, London, Memoirs* **21**, 281–306.
- Eichelberger, J. C., Carrigan, C. R., Westrich, H. R. & Price, R. H. (1986). Non-explosive silicic volcanism. *Nature* **323**, 598–602.
- Fenn, P. M. (1977). The nucleation and growth of alkali feldspars from hydrous melt. *Canadian Mineralogist* **15**, 135–161.
- Gardner, C. A., Cashman, K. V. & Neal, C. A. (1998). Tephra-fall deposits from the 1992 eruption of Crater Peak, Alaska: Implications of clast textures for eruptive processes. *Bulletin of Volcanology* **59**, 537–555.
- Gardner, J. E., Hilton, M. & Carroll, M. R. (1999). Experimental constraints on degassing of magma: isothermal bubble growth during continuous decompression from high pressure. *Earth and Planetary Science Letters* **168**, 201–218.
- Geschwind, C. H. & Rutherford, M. J. (1995). Crystallization of microlites during magma ascent: the fluid mechanics of 1980–1986 eruptions at Mount St Helens. *Bulletin of Volcanology* **57**, 356–370.
- Gibb, F. G. F. (1974). Supercooling and crystallization of plagioclase from a basaltic magma. *Mineralogical Magazine* **39**, 641–653.

- Gondé, C., Martel, C., Pichavant, M. & Bureau, H. (2011). *In situ* bubble vesiculation in silicic magmas. *American Mineralogist* **96**, 111–124.
- Hammer, J. E. (2004). Crystal nucleation in hydrous rhyolite: experimental data applied to classical theory. *American Mineralogist* **89**, 1673–1679.
- Hammer, J. E. & Rutherford, M. J. (2002). An experimental study of the kinetics of decompression-induced crystallization in silicic melt. *Journal of Geophysical Research—Solid Earth* **107**, ECV8 1–23.
- Hammer, J. E., Cashman, K. V., Hoblitt, R. P. & Newman, S. (1999). Degassing and microlite crystallization during pre-climactic events of the 1991 eruption of Mt. Pinatubo, Philippines. *Bulletin of Volcanology* **60**, 355–380.
- Hammer, J. E., Cashman, K. V. & Voight, B. (2000). Magmatic processes revealed by textural and compositional trends in Merapi dome lavas. *Journal of Volcanology and Geothermal Research* **100**, 165–192.
- Higgins, M. D. (1994). Numerical modelling of crystal shapes in thin-sections: estimation of crystal habit and true size. *American Mineralogist* **79**, 113–119.
- Hoblitt, R. P. & Harmon, R. S. (1993). Bimodal density distribution of cryptodome dacite from the 1980 eruption of Mount St. Helens, Washington. *Bulletin of Volcanology* **55**, 421–437.
- Holtz, F., Pichavant, M., Barbey, P. & Johannes, W. (1992). Effects of H₂O on liquidus phase relations in haplogranite system at 2 and 5 kb. *American Mineralogist* **77**, 1223–1241.
- Hort, M. (1998). Abrupt change in magma liquidus temperature because of volatile loss or magma mixing: effects on nucleation, crystal growth and thermal history of the magma. *Journal of Petrology* **39**, 1063–1076.
- James, P. F., Iqbal, Y., Jais, U. S., Jordery, S. & Lee, W. E. (1997). Crystallisation of silicate and phosphate glasses. *Journal of Non-Crystalline Solids* **219**, 17–29.
- Jaupart, C. & Allègre, C. J. (1991). Gas content, eruption rate and instabilities of eruption regime in silicic volcanoes. *Earth and Planetary Science Letters* **102**, 413–429.
- Jaupart, C. & Tait, S. (1990). Dynamics of eruptive phenomena. In: Nicholls, J. & Russell, J. K. (eds) *Modern Methods of Igneous Petrology: Understanding Magmatic Processes*. Mineralogical Society of America, *Reviews of Mineralogy* **24**, 213–238.
- Knoche, R., Dingwell, D. B. & Webb, S. L. (1995). Melt densities for leucogranites and granitic pegmatites: partial molar volumes for SiO₂, Al₂O₃, Na₂O, K₂O, Li₂O, Rb₂O, Cs₂O, MgO, CaO, SrO, BaO, B₂O₃, P₂O₅, F₂O, TiO₂, Nb₂O₅, Ta₂O₅, and WO₃. *Geochimica et Cosmochimica Acta* **59**, 4645–4652.
- Larsen, J. F. (2006). Rhyodacite magma storage conditions prior to the 3430 yBP caldera-forming eruption of Aniakchak volcano, Alaska. *Contributions to Mineralogy and Petrology* **152**, 523–540.
- Launeau, P. & Cruden, A. (1998). Magmatic fabric acquisition mechanisms in a syenite: Results of a combined anisotropy of magnetic susceptibility and image analysis study. *Journal of Geophysical Research—Solid Earth* **103**(B3), 5067–5089.
- Launeau, P. & Robin, P. Y. (1996). Fabric analysis using intercept method. *Tectonophysics* **267**, 91–119.
- Lofgren, G. (1974). An experimental study of plagioclase crystal morphology: isothermal crystallization. *American Journal of Science* **274**, 243–273.
- Lofgren, G. (1980). Experimental studies on the dynamic crystallization of silicate melt. In: Hargraves, R. B. (ed.) *Physics of Magmatic Processes*. Princeton, NJ: Princeton University Press, pp. 487–565.
- Mangan, M. & Sisson, T. (2000). Delayed, disequilibrium degassing in rhyolite magma: decompression experiments and implications for explosive volcanism. *Earth and Planetary Science Letters* **183**, 441–455.
- Martel, C. (2012). Eruption dynamics inferred from microlite crystallization experiments: Application to Plinian and dome-forming eruptions of Mt Pelée (Martinique, Lesser Antilles). *Journal of Petrology* **53**, 699–725.
- Martel, C. & Bureau, H. (2001). *In situ* high-pressure and high-temperature bubble growth in silicic melts. *Earth and Planetary Science Letters* **191**, 115–127.
- Martel, C. & Schmidt, B. C. (2003). Decompression experiments as an insight into ascent rates of silicic magmas. *Contributions to Mineralogy and Petrology* **144**, 397–415.
- Martel, C., Pichavant, M., Bourdier, J., Traineau, H., Holtz, F. & Scaillet, B. (1998). Magma storage conditions and control of eruption regime in silicic volcanoes: experimental evidence from Mt. Pelée. *Earth and Planetary Science Letters* **156**, 89–99.
- Martel, C. & Poussineau, S. (2007). Diversity of eruptive style inferred from the microlites of Mt. Pelée andesite (Martinique, Lesser Antilles). *Journal of Volcanology and Geothermal Research* **166**, 233–254.
- Martel, L., Allix, M., Millot, F., Sarou-Kanian, V., Véron, E., Ory, S., Massiot, D. & Deschamps, M. (2011). Controlling the size of nano-domains in calcium aluminosilicate glasses. *Journal of Physical Chemistry C* **115**, 18935–18945.
- Melnik, O. & Sparks, R. S. J. (1999). Nonlinear dynamics of lava dome extrusion. *Nature* **402**, 37–41.
- Morgan, D. J. & Jerram, D. A. (2006). On estimating crystal shape for crystal size distribution analysis. *Journal of Volcanology and Geothermal Research* **154**, 1–7.
- Mourtada-Bonnefoi, C. & Laporte, D. (2002). Homogeneous bubble nucleation in rhyolitic magmas: an experimental study of the effect of H₂O and CO₂. *Journal of Geophysical Research* **107**(B4), doi:10.1029/2001JB000290.
- Mourtada-Bonnefoi, C. & Laporte, D. (2004). Kinetics of bubble nucleation in a rhyolitic melt: an experimental study of the effect of ascent rate. *Earth and Planetary Science Letters* **218**, 521–537.
- Mullineaux, D. R. & Crandell, D. R. (1981). The eruptive history of Mount St. Helens. In: Lipman, P. W. & Mullineaux, D. R. (eds) . *US Geological Survey, Professional Papers* **1250**, 3–15.
- Muncill, G. E. & Lasaga, A. C. (1987). Crystal-growth kinetics of plagioclase in igneous systems: one-atmosphere experiments and application of a simplified growth-model. *American Mineralogist* **72**, 299–311.
- Muncill, G. E. & Lasaga, A. C. (1988). Crystal-growth kinetics of plagioclase in igneous systems: isothermal H₂O-saturated experiments and extension of a growth model to complex silicate melts. *American Mineralogist* **73**, 982–992.
- Müller, E., Heide, K. & Zanutto, E. D. (1992). Influence of cation coordination on nucleation in silicate-glasses. *Zeitschrift für Kristallographie* **200**, 287–294.
- Navon, O., Chekhmir, A. & Lyakhovsky, V. (1998). Bubble growth in highly viscous melts: theory, experiments, and autoexplosivity of dome lavas. *Earth and Planetary Science Letters* **160**, 763–776.
- Newhall, C. G., Daag, A. S., Delfin, F. G., Jr, Hoblitt, R. P., McGeehin, J., Pallister, J. S., Regalado, M. T. M., Rubin, M., Tubianosa, B. S., Tamayo, R. A., Jr & Umbal, J. V. (1996). Eruptive history of Mount Pinatubo. In: Newhall, C. G. & Punongbayan, R. S. (eds) *Five and Mud*. Seattle, WA: University of Washington Press, pp. 165–195.
- Newman, S. & Lowenstern, J. B. (2002). VOLATILECALC: a silicate melt–H₂O–CO₂ solution model written in Visual Basic for Excel. *Computers and Geosciences* **28**, 597–604.
- Pichavant, M. (1987). Effects of B and H₂O on liquidus phase relations in the haplogranite system at 1 kbar. *American Mineralogist* **72**, 1056–1070.

- Pupier, E., Duchene, S. & Toplis, M. J. (2008). Experimental quantification of plagioclase crystal size distribution during cooling of a basaltic liquid. *Contributions to Mineralogy and Petrology* **155**, 555–570.
- Roobol, M. J. & Smith, A. L. (1976). Mount Pelée, Martinique—Pattern of alternating eruptive styles. *Geology* **4**, 521–524.
- Roselle, G. T., Baumgartner, L. P. & Chapman, J. A. (1997). Nucleation-dominated crystallization of forsterite in the Ubehebe peak contact aureole, California. *Geology* **25**, 823–826.
- Roskosz, M., Toplis, M. J., Besson, P. & Richet, P. (2005). Nucleation mechanisms: A crystal-chemical investigation of phases forming in highly supercooled aluminosilicate liquids. *Journal of Non-Crystalline Solids* **351**, 1266–1282.
- Rutherford, M. J. (2008). Magma ascent rates. *Minerals, Inclusions and Volcanic Processes* **69**, 241–271.
- Rutherford, M. J. & Gardner, J. E. (2000). Rates of magma ascent. In: Sigurdsson, H. S. (ed.) *Encyclopedia of Volcanoes*. San Diego, CA: Academic Press, pp. 207–218.
- Saul, A. & Wagner, W. (1989). A fundamental equation for water covering the range from the melting line to 1273 K at pressures up to 25000 MPa. *Journal of Physics and Chemistry* **18**, 1537–1565.
- Sparks, R. S. J. (1978). The dynamics of bubble formation and growth in magmas: a review and analysis. *Journal of Volcanology and Geothermal Research* **3**, 1–37.
- Swanson, S. E. (1977). Relation of nucleation and crystal-growth rate to the development of granitic textures. *American Mineralogist* **62**, 966–978.
- Toramaru, A. (1989). Vesiculation process and bubble size distributions in ascending magmas with constant velocities. *Journal of Geophysical Research—Solid Earth* **94**(B12), 17523–17542.
- Toramaru, A. (2001). A numerical experiment of crystallization for a binary eutectic system with application to igneous textures. *Journal of Geophysical Research—Solid Earth* **106**, 4037–4060.
- Tsuchiyama, A. (1983). Crystallization kinetics in the system $\text{CaMgSi}_2\text{O}_6$ – $\text{CaAl}_2\text{Si}_2\text{O}_8$. The delay in nucleation of diopside and anorthite. *American Mineralogist* **68**, 687–698.
- Tuttle, O. F. & Bowen, N. L. (1958). *Origin of Granite in the Light of Experimental Study in the System $\text{NaAlSi}_3\text{O}_8$ – KAlSi_3O_8 – SiO_2 – H_2O* . Geological Society of America, *Memoirs* **74**.
- Wolf, K. J. & Eichelberger, J. C. (1997). Syneruptive mixing, degassing, and crystallization at Redoubt Volcano, eruption of December, 1989 to May 1990. *Journal of Volcanology and Geothermal Research* **75**, 19–37.
- Woods, A. W. & Koyaguchi, T. (1994). Transitions between explosive and effusive eruptions of silicic magmas. *Nature* **370**, 641–644.
- Young, S. R., Sparks, R. S. J., Aspinall, W. P., Lynch, L. L., Miller, A. D., Robertson, R. E. A. & Shepherd, J. B. (1998). Overview of the eruption of Soufrière Hills volcano, Montserrat, 18 July 1995 to December 1997. *Geophysical Research Letters* **25**, 3389–3392.
- Zhang, Y. & Behrens, H. (2000). H_2O diffusion in rhyolitic melts and glasses. *Chemical Geology* **169**, 243–262.